NAVAL POSTGRADUATE SCHOOL

MONTEREY, CALIFORNIA

THESIS

ENGINEERING SUPERHYDROPHOBIC BEHAVIOR IN 3D-PRINTED STAINLESS STEEL COMPOSITES

by

Justin M. Budan

June 2022

Thesis Advisor: Troy Ansell
Co-Advisor: Andy Nieto

THIS PAGE INTENTIONALLY LEFT BLANK

REPORT DOCUMENTATION PAGE			*Form Approved OMB No. 0704-0188*

1. AGENCY USE ONLY *(Leave blank)*	**2. REPORT DATE** June 2022	**3. REPORT TYPE AND DATES COVERED** Master's thesis

4. TITLE AND SUBTITLE
ENGINEERING SUPERHYDROPHOBIC BEHAVIOR IN 3D-PRINTED STAINLESS STEEL COMPOSITES

5. FUNDING NUMBERS

6. AUTHOR(S) Justin M. Budan

7. PERFORMING ORGANIZATION NAME(S) AND ADDRESS(ES)
Naval Postgraduate School
Monterey, CA 93943-5000

8. PERFORMING ORGANIZATION REPORT NUMBER

9. SPONSORING / MONITORING AGENCY NAME(S) AND ADDRESS(ES)
N/A

10. SPONSORING / MONITORING AGENCY REPORT NUMBER

11. SUPPLEMENTARY NOTES The views expressed in this thesis are those of the author and do not reflect the official policy or position of the Department of Defense or the U.S. Government.

12a. DISTRIBUTION / AVAILABILITY STATEMENT
Approved for public release. Distribution is unlimited.

12b. DISTRIBUTION CODE
A

13. ABSTRACT (maximum 200 words)

This thesis discusses the wettability of 316L stainless steel composites using carbon nanotubes and manufactured via a selective laser melting. Superhydrophobicity is created through the combination of low surface tension and surface roughness at a micro to nanoscopic scale, and it has become a topic of vigorous study over the past 20 years. Previous studies have relied primarily on processes such as etching and nanomaterial arrays to generate surface roughness, followed by the application of harmful chemicals (e.g., fluorosilanes) to modify surface energy and achieve superhydrophobicity. Stainless steel powder (316L) was combined with carbon nanotubes, which demonstrate near-hydrophobic properties, via high energy ball milling in attempts to reduce the materials surface energy. An ideal pillared surface geometry based on natural superhydrophobicity was produced through additive manufacturing using multiple concentrations of carbon nanotube composites. Through material characterization including sessile water drop contact angle measurements, optical profilometry, and microscopy, it was determined that all samples remained hydrophilic in nature due to insufficient surface energy modification using carbon nanotubes. However, trends indicate that further increasing CNT concentration, controlling printing laser energy density, and slight model modifications could demonstrate hydrophobic effects.

14. SUBJECT TERMS additive manufacturing, stainless steel, carbon nanotubes, wettability, superhydrophobicity	**15. NUMBER OF PAGES** 111
	16. PRICE CODE

17. SECURITY CLASSIFICATION OF REPORT	**18. SECURITY CLASSIFICATION OF THIS PAGE**	**19. SECURITY CLASSIFICATION OF ABSTRACT**	**20. LIMITATION OF ABSTRACT**
Unclassified	Unclassified	Unclassified	UU

NSN 7540-01-280-5500

Standard Form 298 (Rev. 2-89)
Prescribed by ANSI Std. 239-18

THIS PAGE INTENTIONALLY LEFT BLANK

Approved for public release. Distribution is unlimited.

ENGINEERING SUPERHYDROPHOBIC BEHAVIOR IN 3D-PRINTED STAINLESS STEEL COMPOSITES

Justin M. Budan
Ensign, United States Navy
BS, United States Naval Academy, 2021

Submitted in partial fulfillment of the
requirements for the degree of

MASTER OF SCIENCE IN MECHANICAL ENGINEERING

from the

NAVAL POSTGRADUATE SCHOOL
June 2022

Approved by: Troy Ansell
Advisor

Andy Nieto
Co-Advisor

Garth V. Hobson
Chair, Department of Mechanical and Aerospace Engineering

THIS PAGE INTENTIONALLY LEFT BLANK

ABSTRACT

This thesis discusses the wettability of 316L stainless steel composites using carbon nanotubes and manufactured via a selective laser melting. Superhydrophobicity is created through the combination of low surface tension and surface roughness at a micro to nanoscopic scale, and it has become a topic of vigorous study over the past 20 years. Previous studies have relied primarily on processes such as etching and nanomaterial arrays to generate surface roughness, followed by the application of harmful chemicals (e.g., fluorosilanes) to modify surface energy and achieve superhydrophobicity. Stainless steel powder (316L) was combined with carbon nanotubes, which demonstrate near-hydrophobic properties, via high energy ball milling in attempts to reduce the materials surface energy. An ideal pillared surface geometry based on natural superhydrophobicity was produced through additive manufacturing using multiple concentrations of carbon nanotube composites. Through material characterization including sessile water drop contact angle measurements, optical profilometry, and microscopy, it was determined that all samples remained hydrophilic in nature due to insufficient surface energy modification using carbon nanotubes. However, trends indicate that further increasing CNT concentration, controlling printing laser energy density, and slight model modifications could demonstrate hydrophobic effects.

THIS PAGE INTENTIONALLY LEFT BLANK

TABLE OF CONTENTS

LIST OF FIGURES

LIST OF TABLES

THIS PAGE INTENTIONALLY LEFT BLANK

LIST OF ACRONYMS AND ABBREVIATIONS

ABS	acrylonitrile butadiene styrene
AM	additive manufacturing
ASTM	American Society of Testing and Materials
BPR	ball to powder ratio
CA	contact angle
CAD	computed aided drafting
CNT	carbon nanotubes
DE	diatomaceous earth
ED	energy density
GDP	gross domestic product
HEBM	high energy ball mill
LPBF	laser powder bed fusion
SEM	scanning electron microscope
SLM	selective laser melting

THIS PAGE INTENTIONALLY LEFT BLANK

ACKNOWLEDGMENTS

This work could not have been possible without the contributions and hard work of so many people within my life. First, I would like to thank my advisors, Dr. Troy Ansell and Dr. Andy Nieto, for all of their hard work in assisting me through every step of the process. This thesis would not have been possible without them. I would also like to thank the many staff and faculty members in the mechanical engineering department at the Naval Postgraduate School who assisted me in every setback and difficulty that came up. Thank you to Stefan Kohlgrueber for teaching me everything that I needed to know about operating the EOS printer, and always being there to help when there were setbacks in the printing process. Thank you to Dr. Dragoslav Grbovic and Dr. Claudia Luhrs for giving the training and experience that I needed to operate the tools necessary to achieve all the experiments. Thank you to Dr. Chanman Park for keeping a watchful eye on my safety and assisting me in preparing all of my samples for microscopy. Thank you to Dr. Emre Gunduz for all he taught me about additive manufacturing that I was able to apply to this work. Thank you to all the staff and support team that provided me with an amazing research experience at the Naval Postgraduate School this year.

In addition to the staff, I would like to thank many of the friends that I have met in this experience. Thank you to Sam Rice, David Tauber, K.M. Phua, and Maggie Ruud for bringing a smile to my face every day in the lab. Thank you to the members of Boy Scout Troop 43 for giving me the opportunity to have a creative outlet in Monterey outside of classes. Thank you to Prajna Jalagam for your hard work in laying a quality foundation prior to me beginning this research.

This work is dedicated to my amazing fiancé, Sarah, as well as the most sacred heart of Jesus.

THIS PAGE INTENTIONALLY LEFT BLANK

I. MOTIVATION

A. CORROSION RESISTANCE

Corrosion is currently one of the most significant economic and engineering barriers in the Navy, the United States, and the entire world. In 2013, the cost of corrosion was estimated to be the equivalent of 3.4% of the global gross domestic product (GDP), coming out to approximately 2.5 trillion U.S. dollars [1]. This aligns with trends over the past decade showing the direct costs of corrosion to consume between 3% and 5% of a nation's GDP [2]. In 2016, it was estimated that the Department of Defense (DOD) spent in excess of $20.6 billion on corrosion related repairs and issues [3]. With the Navy and Marine Corps annual maintenance budget absorbing large portions of these costs, corrosion prevention could have a high economic impact.

Corrosion is defined as "the destructive attack of a material by its reaction with the environment" [4]. Particularly, this takes the form of a metal converting to a more stable state through oxidation and reduction chemical reactions. This process, outlined in Figure 1, requires four primary factors to be present: an anodic material, a cathodic material, a path for electrons to move between the anode and the cathode, and an electrolytic solution [4]. In a majority of metallic materials, corrosion is most likely to occur in a maritime environment rich in saltwater and warm temperatures, common areas of operation for U.S. Navy and Marine Corps forces [2], leading to numerous methods of corrosion prevention. In order to control corrosion, one must modify or eliminate one of these conditions. Methods range from adding large blocks of anodic material to the hull of a ship to control the location of corrosion, to application of new coatings and designs for optimal performance in a variety of conditions [4]. Corrosion remains a consistent and expensive opponent against the United States Navy, however, and new methods of suppressing and eliminating this process are necessary.

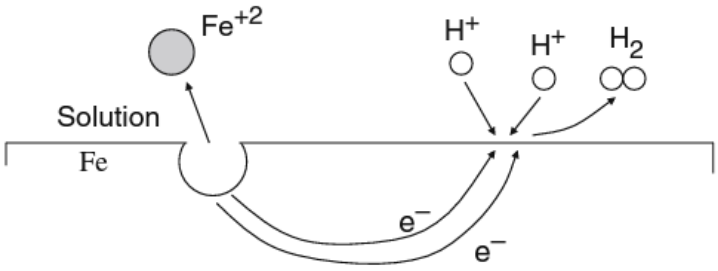

Figure 1. Diagram of hydrogen evolution corrosion for iron in solution. Source: [4].

Near the turn of the 21st century, researchers began to view superhydrophobicity as a potential means to mitigate corrosion. A superhydrophobic surface is defined as one where a water droplet makes a > 150° angle on contact with the surface (i.e., contact angle) [5]. This trait to promote self-cleaning can be found in plants such as the lotus leaf and rose petals, as well as in animals such as water striders, which have hydrophobic properties in their legs to allow them to walk on water [5]. Unlike other means of corrosion prevention previously discussed (e.g., utilizing sacrificial anodes or unique coatings), superhydrophobicity aims to reduce the corrosion by minimizing contact between water molecules and the corrodible surface. Most studies indicate that an increase in hydrophobicity will lead to a decrease in corrosion due to this minimization of material-solution interactions [6]–[8]. Achieving this hydrophobic state is heavily reliant on the chemical nature of the material as well as the surface roughness and geometry. This has led to a wide variety of approaches over the past decade to utilize superhydrophobicity as a means of preventing corrosion. These studies will be discussed in greater detail throughout this report. When properly implemented, superhydrophobicity is a viable defense against the corrosion of metals in many applications.

B. ADDITIONAL USES OF SUPERHYDROPHOBICITY

Although corrosion resistance is the primary motivation for developing superhydrophobic metals in this thesis, there are additional professional and engineering areas of interest for utilizing the trait.

1. Surface Drag Reduction

Due to the surface slip conditions that result from superhydrophobic surfaces, superhydrophobicity may be used as a means of skin friction drag or surface drag reduction. Drag is defined as the force that opposes the direction of an object moving through a fluid and consists of two types. These types include form drag generated by a solid object's macroscopic geometry, forcing a fluid to change flow directions. This form of drag is also commonly referred to as pressure drag. The other is skin friction drag, defined by the inability of a fluid to "smoothly" slip across a solid surface due to both friction and fluid viscosity [9]. This form of drag is often modelled using a "no-slip" condition in which the velocity of a fluid is zero along the solid surface of an object. The resulting shear force opposes the movement of the flow with an equal and opposite resistive force on the surface. When water comes into contact with a superhydrophobic material, the water will roll or glide across the surface in comparison to sticking to the surface and generated friction. Without this friction creating a no-slip type of condition, the fluid is able to freely roll or glide across the surface of the object and skin friction is greatly reduced [9]. Figure 2 shows an example of the difference that superhydrophobicity could make in skin friction by modifying the fluid velocity profile across the surface layer of fluid. The first image represents standard no slip conditions, and the middle represents some of the slip that could result from hydrophobicity. Since surface drag is derived based upon the difference between surface velocity and average velocity, the vertical line on the right image would correspond to no skin friction. If a boat or submarine was able to reduce their surface drag, even marginally, this could greatly reduce fuel cost as well as potentially increase vehicle speed and agility.

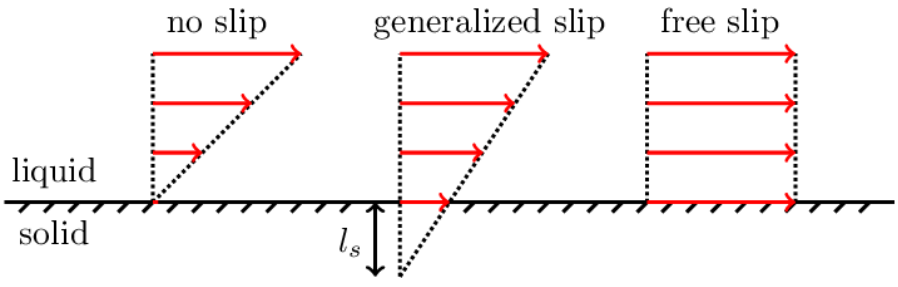

Figure 2. Fluid dynamics model of skin friction under no slip, generalized slip, and free slip. Source [10].

2. De-icing Capabilities

The ability of superhydrophobic materials to repel water would also reduce the adhesion of ice to the material's surface [5]. This would have distinct advantages in the aviation field where large pieces of ice can have severe negative effects on the performance of planes [11]. If microscopic ice particles are not able to stick and form on a surface where they would otherwise develop and further crystallize, the risk of large ice shards disrupting the turbines or compressors in aircraft engine is minimized. This capability is seen in everyday life through treatments for car windshields with products such as Rain-X®. In addition to preventing excessive streaking on car windows, such substances are often applied at the beginning of the winter months in order to reduce the effort necessary to scrape ice off of the windshield. Superhydrophobic materials often takes advantage of both the low electrostatic attraction between the droplet and object alongside the air pockets that could form between the droplet and object to achieve de-icing capabilities. With air pockets, the primary means of heat transfer is air convection as opposed to direct thermal conductivity. This reduces the likelihood of ice crystals forming on the surface unless they are already forming in air [5]. If these ice crystals do form, gravitational forces are likely to overcome the bonding forces between the surface as the water droplets or ice crystals and slide off of the surface prior to creating excessive torque or damage on any systems.

3. Medical Applications

In the medical field, especially in surgery, one of the biggest risks to patients is the risk of infections corresponding to treatment. Modern medicine has made great strides to reduce the risk of post-operative infections through strict sanitary protocols, but the implementation of superhydrophobic material could further assist in this process. Many illnesses in the form of viruses and bacteria, regardless of size, are water-borne in nature. If materials such as scalpels and other surgical tools utilize hydrophobic treatments, the risk of illness traveling through the material is reduced. Additionally, the corrosion-resistant properties found in superhydrophobic materials make them ideal candidates for implants and other biomedical instruments. In some cases, the treatments used to create hydrophobicity can also repel hydrocarbons such as lipids, further improving medical

functionality [12]. This is certainly a solution that would not come without potential disadvantages, as the risk must be minimized of any foreign chemicals used in hydrophobic treatment degrading or entering the body. To use superhydrophobicity in the medical field, as well as any environmentally conscious tasks, a novel approach must be taken to the develop such materials without use of strong or hazardous chemicals with potential unintended consequences [12].

C. ADVANTAGES OF ADDITIVE MANUFACTURING

Additive manufacturing (AM) is defined by the American Society for Testing and Materials (ASTM) as "the process of joining materials to make objects from 3D model data, usually layer upon layer, as opposed to subtractive manufacturing technologies" [13]. AM provides the user with several key advantages that may not be easily replicable in other manufacturing processes including the use of a wide variety of materials, complex part geometry fabrication capabilities, and limited technical expertise necessary. AM methods such as the selective laser melting (SLM) show a wide range material compatibility in metals. Most metals can be fabricated into parts if they are able to be processed in a powder form and can then be properly fused using a laser without disrupting other material properties. This allows for a variety of alloys and unique composites to manufactured in this way, leading to the ability to produce samples with limitless combinations of properties, including wettability. Additionally, AM methods allow the creation of very abstract and detailed geometries that are not easily reproducible in most large-scale metal manufacturing. When details such pillared geometries and surface roughness are vitally important, this advantage may be crucial when developing a hydrophobic metal capable of rapid production. Lastly, AM does not require the chemical or technical expertise that would otherwise be necessary with other means of achieving superhydrophobic results [13]. If the capability existed to apply an engineered micro-structured surface to a computed automated drafting (CAD) file and print using a prefabricated alloy powder, this could open the uses of superhydrophobicity to the limits of the user's imagination and revolutionize its applications in the world.

THIS PAGE INTENTIONALLY LEFT BLANK

II. BACKGROUND

A. SUPERHYDROPHOBICITY AND NATURE

1. Wettability and Introduction to Hydrophobicity

All surfaces possess a certain level of wettability. Wettability is the material property that describes its level of electrostatic attraction with water. This material property, wettability, is dominated by the bonding energies and polar forces that binds water molecules to each other, as well as water molecules to the surface of an object. If water has a significantly stronger attraction to an object than itself, it will immediately spread out on contact with the surface in order to maximize the surface area contact. Meanwhile, if the object was not attracted to the water or possibly even slightly repelled by water, it would reduce its surface contact with the material to a minimum by maintaining a spherical shape. In order to quantify and measure this property of wettability, scientists observe the amount of contact that a water droplet makes with a surface and measures this angle (contact angle). As Figure 3 demonstrates, a contact angle is a measurement of the angle between the surface and a water droplet. A contact angle lower than 90° would correspond to a hydrophilic material, or a material with high wettability. A contact angle higher than 90° would correspond to a hydrophobic material and possesses low wettability. This scale of contact angles ranges from 0 to 180 degrees, with 90° generally serving as the line between hydrophobic and hydrophilic material. However, the geometric surface properties are not particularly advantageous in materials until superhydrophobicity is achieved. The benchmark for achieving superhydrophobicity in a material is 150°or more, as well as a contact angle hysteresis of less than 10 degrees [5].

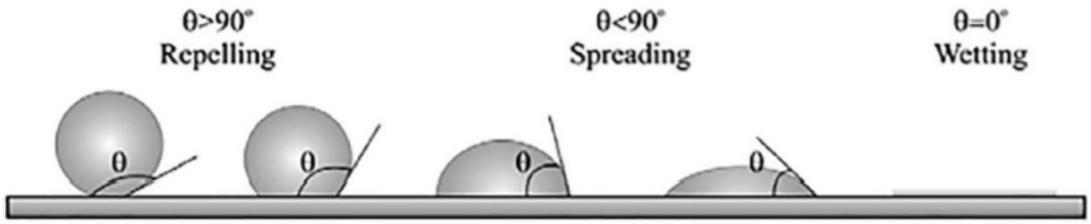

Figure 3. Demonstration of different levels of wettability on a flat surface. Source: [5].

Contact angle hysteresis and roll off angles are a slightly different concepts to traditional contact angle measurements but are equally valuable in determining the hydrophobic nature of a material. Contact angle hysteresis is defined as the maximum difference that could occur between the advancing and receding contacts angles prior to rolling [14]. These advancing and receding contact angles are the results of a fluid droplet being at an angle, which effects the contact angle of both sides of the droplet as seen in Figure 4. Because this hysteresis is nearly always associated with the droplet being placed at an angle and rolling away, it is often used synonymously with the roll off angle. The roll off angle is defined as the minimum angle required to induce a water droplet to roll down an incline [14]. This is best described in the low contact angle hysteresis and roll off angle on many plants that utilize superhydrophobicity for the benefit of self-cleaning. If a superhydrophobic leaf is positioned at as little as a 5° angle from the ground, water droplets will roll across a leaf and pick up any small particulates or debris from the plant prior to falling off the leaf as opposed to sticking and weighing the plant down.

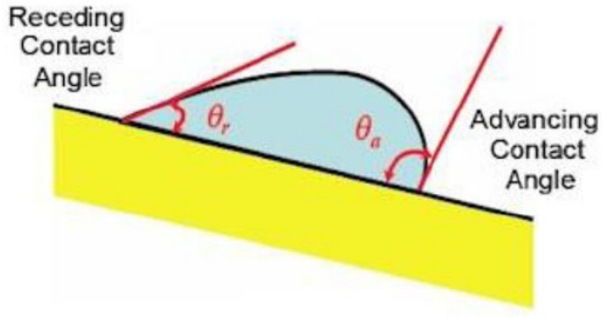

Figure 4. Contact angle hysteresis on a sloped surface. Source: [14].

2. Governing Equations of Wettability

The wettability of a material is guided by three governing equations, each of which takes into account a new variable when determining the resultant contact angle between a particular fluid and material. The first of these is defined as Young's equation, which is defined as the following.

$$\cos\left(\theta_y\right) = \frac{\gamma_{sv} - \gamma_{sl}}{\gamma_{lv}} \tag{1}$$

In this equation, θ_y corresponds to the contact angle between the material and the droplet, and the different γ values correspond to different surface energies or surface tensions. γ_{sv} corresponds to the solid (surface) and vapor (air) interaction, γ_{sl} corresponds to the solid liquid (water) interaction, and γ_{sl} corresponds to the liquid vapor interaction [5], [14]. If one operates under the assumption that the properties of both the liquid and surrounding gas are not going to vary from water and air, the only variables that one would be able to modify to affect the contact angle would be the surface energy of the material, γ_{sl} and γ_{sv}. Based off Young's equation, the determination of hydrophobic or hydrophilic is dependent on which is greater, the surface tension between the surface and air or between the surface and water. This surface tension is a major element of success for achieving hydrophobicity, but experiments that are able to achieve superhydrophobicity indicates that other variables must be taken into account beyond surface energies [5]. Experiments have achieved contact angles higher than what is possible under this governing equation alone. This was done though modifying the geometry and roughness of the surface, which led to a modification of the governing equation by Wentzel.

Building upon Young's equation is the Wentzel equation, defined by Equation 2, where θ_w corresponds to the new contact angle, θ_y shows the contact angle calculated under Young's equation, and r is the surface roughness factor [5], [14]. This factor is larger than 1 and is proportional to the actual surface area over the projected surface area [5].

$$\cos\left(\theta_w\right) = r * \cos\left(\theta_y\right) = \frac{r*\left(\gamma_{sv} - \gamma_{sl}\right)}{\gamma_{lv}} \tag{2}$$

Equation 2 is meant to take into effect the roughness of a material when computing its wettability. This becomes very important when engineering materials with wettability in mind, as increasing roughness can amplify both hydrophobicity and hydrophilicity depending on the starting wettability condition [14]. This is grounded in the Wentzel equation, as the roughness factor is always a value greater than 1 and will amplify the magnitude regardless of its sign (i.e., positive or negative value). For this reason, the chemical properties of a material cannot be overlooked and superhydrophobicity is not able to be achieved with geometry alone. An example of how roughness amplifies both hydrophobicity and hydrophilicity is demonstrated in Figure 5, which shows how a water droplet would react to both hydrophobic and hydrophilic materials in a cone array. A hydrophilic material would demonstrate what is known as the wicking effect where the water droplet will begin to sink into the pillar to maximize surface contact and minimize contact angle. Likewise, a hydrophobic material will try to reduce its surface area and the droplet will attempt to rest on the tip of the pillar [14].

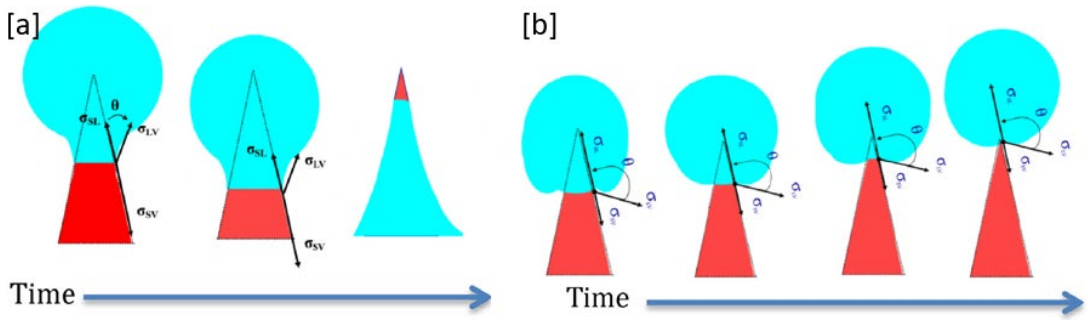

Figure 5. Water droplet demonstrating the wicking effect on a hydrophobic pillared surface (a), and water droplet rising to the tip of a hydrophobic pillar (b). Source: [14].

The Wentzel equation explains the vast majority of hydrophobic phenomena, but it does not fully capture the complexity of situations such as that of a water strider where air pockets are used between water droplets and the surface to enhance hydrophobicity. To

take trapped air into effect, the final form of the equation used to define wettability is found in the form of the Cassie-Baxter equation, written as follows.

$$\cos\left(\theta_{CB}\right) = r * f_S * \cos\left(\theta_y\right) + f_S - 1 \tag{3}$$

This model, much like the Wentzel equation, builds upon previous iterations of wettability. The only new variable in this equation is f_s, which is a constant defined as the ratio of solid to liquid interface to the entire interface within the projected surface area [5], [14]. This constant varies from zero, where a water droplet is completely suspended in air, to one where there is no air pocket supporting the water droplet [5]. Having an air pocket is an important measure in superhydrophobic materials, as the chemical properties of materials is only able to generate hydrophobicity alone [14]. The situations in which each of these equations are best used can be seen in Figure 6. In many circumstances surrounding superhydrophobicity without an air pocket, the constant f_s would have a value of one, which would revert this equation back to the Wentzel equation. If the surface is completely smooth, the value of r would also be one and Young's equation can accurately define the hydrophobicity of the material.

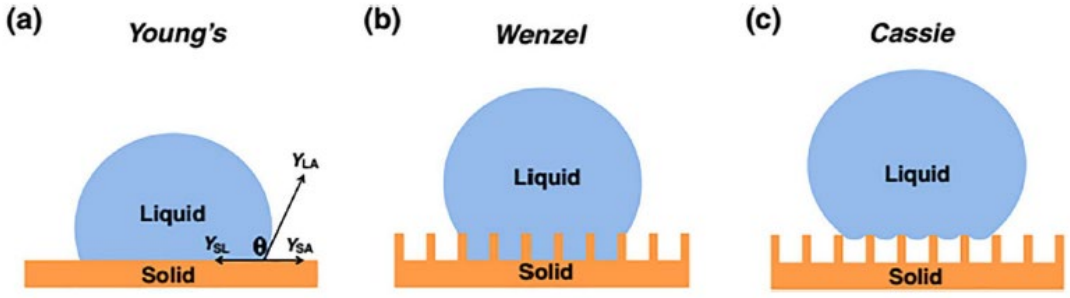

Figure 6. Model of wettability equations. Source: [14].

3. Superhydrophobicity in Nature

When looking for an example of superhydrophobicity, one can first look to the various examples which are found in nature. Since the idea of the "Lotus effect" was coined as early as 1992 [15], the lotus has become representative of superhydrophobicity and its

self-cleaning capabilities. Some lotus leaves are capable of achieving water contact angles between 150° and 165° alongside several other species such as some Eucalyptus leaves and possesses contact angle hysteresis that allow water to “fall off” or “roll away” from the leaf better than nearly everything else in nature [15]. The reason for the lotus leaf’s success is a combination of wax on the surface of the leaf alongside its unique micro- and nano-structure. When one looks at a lotus or eucalyptus leaf or rose petal or any comparable species, it appears very smooth to the human eye, but their roughness plays a crucial role in their ability to repel water. When looking at the microstructure of these plants under a scanning electron microscope (SEM), many species have cone structures on the surface which are covered in a wax to optimize both the chemical properties needed and geometric roughness necessary to support superhydrophobicity [15].

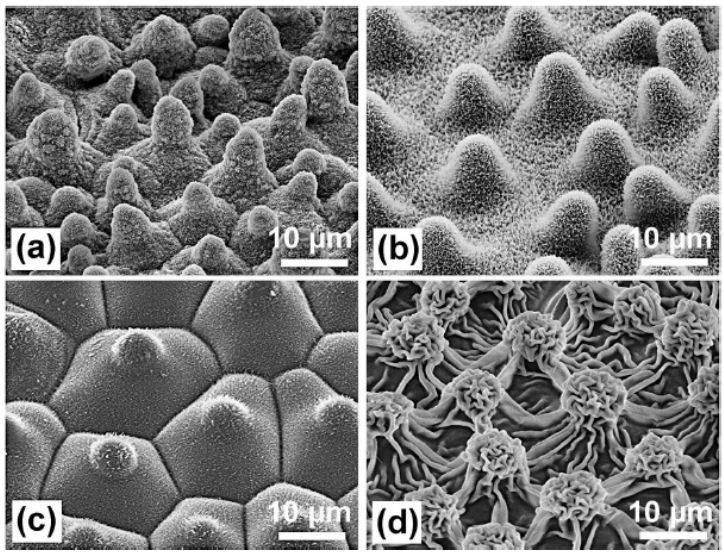

Figure 7. SEM image of various plants, including lotus leaf (a).
Source: [15].

A unique element of the lotus leaf in addition to its papillae wax is that the size and height of these microscopic cones on the surface are highly variable. When compared to the other leaves in Figure 7[b-d], the lotus leaf shows smaller and tighter cone structures, but also a large variation in height that generates an enhanced roughness. This is not an easily replicated design in manufacturing, but has its advantages in a natural environment

for repelling rainwater [15]. With a variable cone height, each of the cones are able to act in a slightly different manner as expressed in Figure 8. Water droplets would normally sit atop the highest pillars due to their superhydrophobic condition, but this varies under the momentum of a rain drop. The lotus leaf is designed in a way to effectively absorb the momentum of rain drops without risk of damaging the surface. In the event of a rain drop, momentum would cause the droplet to fall beyond the top layer and create a high water contact surface area and subsequent repelling force on the pillars labelled re. Since the cone height is variable, there would be another layer of cones for the water to rest upon once the high peaks slow the momentum (labelled n). The cones below would slightly adhere to the water droplet due to its bonding energy and further stabilize the droplet (labelled ad) until all momentum as absorbed [15]. When combined with a sufficient air pocket, this allows the lotus leaf to have the superhydrophobic self-cleaning qualities that have led to it being a symbol of purity for the past several centuries.

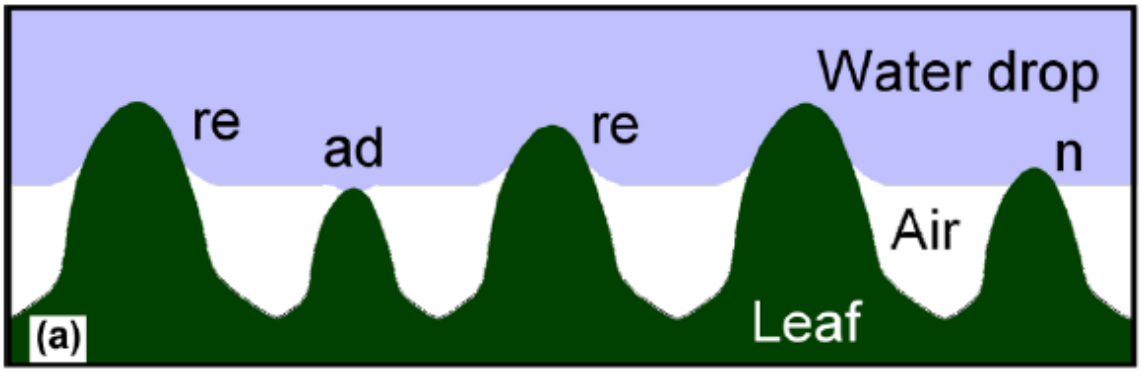

Figure 8. Superhydrophobic basis in lotus leaf. Source: [15].

The methods used in the lotus leaf are not unique to plant species, as the same principles are present in animals such as the water strider to allow them to walk on water. These species rely primarily on their ability to trap air in between the main material of their legs and the water, creating a small air bubble that they walk on. Since the bug itself is lightweight, these air bubbles allow the water strider to achieve a superhydrophobic state based on the effects of the Cassie-Baxter equation and is able to glide across the water without flying or sinking [14].

B. ENGINEERING OF SUPERHYDROPHOBIC MATERIALS

Previous experiments aimed at generating hydrophobic materials, particularly in metallic surfaces, rely primarily on processes like plasma and chemical etching, electrodeposition, and others [16].

1. Methods of Generating Superhydrophobic Roughness

a. Templating

Templating is a method of generating hydrophobicity in which a mold of superhydrophobic geometry is used to replicate micro and nanoscopic roughness onto another part [5]. This form of treatment is very similar to the casting method used in metals in which a molten metal is formed in a mold. The biggest difference is that this mold has the geometric features necessary to amplify roughness without interfering with any dimensional qualities. Figure 9 demonstrates the templating process used by Peng *et al.* [5] to replicate the geometry of a superhydrophobic leaf into a polymer film that was able to generate superhydrophobic results. There is no evidence in the successful implementation of superhydrophobic templating in metals without non-metal coatings, likely due to the difficulty of finding metals whose surface energy allows them to be hydrophobic in nature.

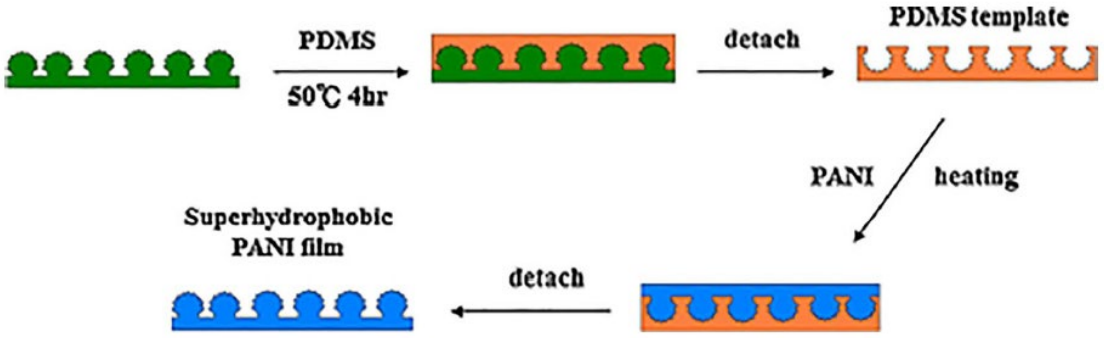

Figure 9. Superhydrophobic templating process. Source: [5].

b. Etching

Etching in various forms makes up a large majority of attempts at producing superhydrophobic materials. Etching is used to attack weak areas of a structure or crystal,

often along crystal planes, which allows for roughness to be generated at the crystalline size or smaller. Etching can be divided into dry and wet etching. Dry etching relies on the use of a plasma or ion beams which react in destructive way on the surface to roughen it. These methods are effective in roughening surfaces at a microscopic and nanoscopic level but are reliant upon extremely precise instrumentation that is not readily available. Wet etching is reliant on the use of chemicals such as strong acids to destroy regions of high energy dislocation sites to generate roughness [5]. Although these chemicals are often readily available and inexpensive in production, many of these acids and other chemicals are toxic and not environmentally friendly [7]. In using additive manufacturing techniques to produce roughness, there is hope that no chemical processes or expensive methods are needed to produce a superhydrophobic material.

c. Electrodeposition and Anodization

Two additional processes that can be used in producing a superhydrophobic material include electrodeposition and anodization. Both processes rely heavily on the principles of corrosion. In anodization, the anode will begin to react while immersed in an oxygen-rich electrolytic solution to produce a rough oxidation layer that can be controlled by the user. This is often considered a fast and inexpensive method for producing surface roughness, but the process is still generally reliant in the use of chemicals or coatings with low surface energy to be applied to the oxide layer [5]. Electrodeposition is a similar concept to anodization, except this process is more reliant on the reactions of the cathode. In the case of electrodeposition, a cathode is plated or covered in a rough coating of the negatively charged anions surrounding the cathode. This can be done with the anions being produced by the anode in a controlled environment, or another material based in the electrolyte that the solution is immersed in [5]. Much like anodization, this process does not directly create superhydrophobicity, but rather the roughness amplifies hydrophobicity. The necessary low surface energy coatings or chemicals must still be applied in this process to generate hydrophobic materials.

d. Diatomaceous Earth Polymer Coatings

A recent attempt at engineering superhydrophobicity involves the use of diatomaceous earth. Diatomaceous earth (DE) is the fossilized exo-skeleton of diatoms, which are "unicellular microscopic plants and inhabit all aquatic and moist environments" [16]. The structures are highly variable and possess the necessary roughness needed to produce superhydrophobic surfaces when combined with proper chemical treatments. DE is in the scale of 1 to 500 microns with many pillars, pores, ridges, and other rough features that greatly impact the surface area [16].

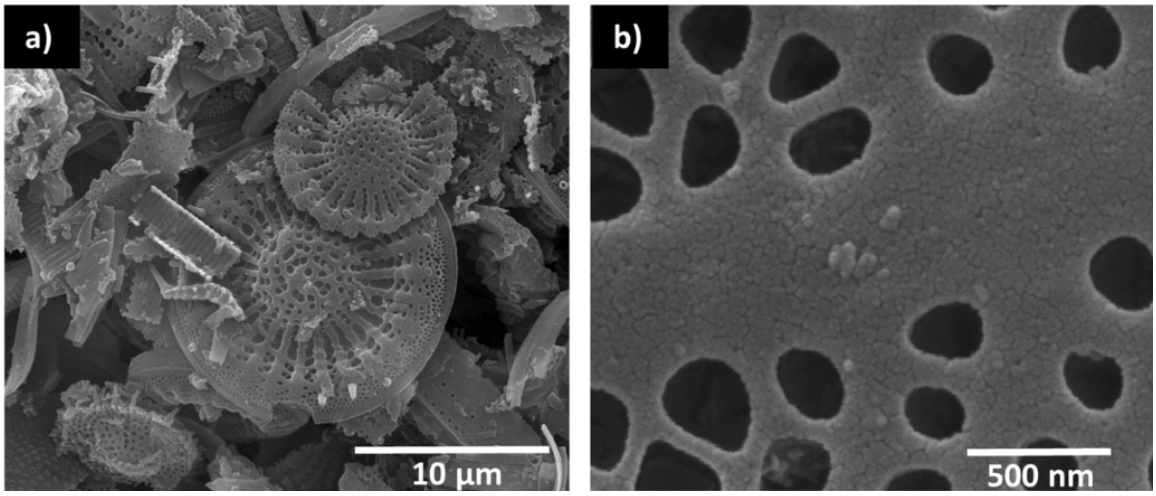

Figure 10. SEM images of white DE particles (a), and magnified SEM image of DE particle (b). Source [16].

Incorporating DE into coatings is a novel approach to improving the geometry and roughness of a sample, as well as improving the chemical properties of the material since a majority of DE has a silicon base. However, many studies using DE required the use of fluorosilanes in the coating process. Fluorosilanes are molecules based on fluorine atoms bonded to each of silicon's four chemical bonds. The molecule is highly toxic. Coupling DE with a fluorosilane chemical treatment turns DE coating into superhydrophobic coatings. Treated DE coatings can be applied on a wide variety of surfaces including polymers, ceramics, and metals as seen in Figure 11, which shows the results of an experiment conducted by Sedai *et al.* to determine the effects of flourosilane on DE's

wettability [16]. Additional studies by Oliveira, Reis, and Mano [17] and Perera *et al.* [18] support these findings and the use of DE coatings.

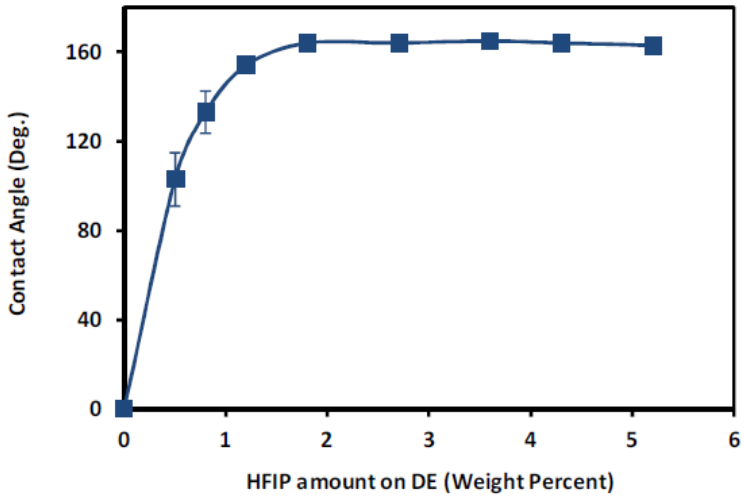

Figure 11. Effects of fluorosilane treatments on DE wettability. Source: [16].

e. Turning Operations

A final approach taken to developing the necessary roughness for superhydrophobicity was through turning operations on a lathe. In an experiment conducted by Zhu and Hu [8], an attempt was made to roughen copper bars using a turning lathe operation to create ribbed tracks on the copper. To create this threading, a 60-degree external thread cutting tool was use with a lathe feed rate ranging from 50 to 200 microns per revolution. When combined with stearic acid, the experiment was able to produce superhydrophobic results. This process is unique in that it is quick, inexpensive, and does not rely on any chemistry to effectively roughen the surface as long as the lathe being used is able to operate at the necessary precision to cut these patterns.

2. Chemicals Used in Hydrophobic Coatings

Regardless of the level of roughness that most materials possess, most materials are hydrophilic in nature. Roughness only amplifies the hydrophobic or hydrophilic nature of

a surface but cannot cross the 90° contact angle threshold. In order to create surfaces that are superhydrophobic, this roughness must be coupled with a low surface energy material that has hydrophobic qualities as a smooth surface. To accomplish this, various chemical treatments and special coatings are commonly used to produce superhydrophobic metals, polymers, and ceramics.

a. Use of Stearic Acid

A common chemical treatment applied to roughened samples is stearic acid. Liu *et al.* [7] applied an 0.1M ethanol solution of stearic acid to a sample of etched copper to produce a superhydrophobic surface of over 150 degrees. The copper used was not hydrophobic prior to treatment, achieving a contact angle slightly above 70 degrees while smooth and decreasing after etching for roughness. The reason that stearic acid is commonly used as a superhydrophobic thin film coating, especially in copper, is because it allows for better corrosion resistance than many alternative chemicals that interfere with the passivation or immunity of copper. This material was also used by Zhu and Hu [8] in their turning operations of copper to produce superhydrophobic copper surfaces, which allowed for an improvement in corrosion resistance for their samples. Stearic acid is one of the most environmentally friendly options available and is effective on copper, but this acid has not been found to promote superhydrophobicity in other materials and is not likely to be beneficial when studying stainless steel and other metals.

b. Use of Silanes and Toxic Chemicals

The use of fluorosilanes is one of the most common chemical treatments in superhydrophobic materials, but the chemicals can create hazards to humans and the environment [7]. Fluorosilanes as well as other varieties of silanes were used in the DE coatings explored in Sedai *et al.* [16] as well as experiments conducted by Latthe *et al.* [19] aimed at developing superhydrophobic steel surfaces. Milionis *et al.* [20] additionally used fluorosilane treatment for generated superhydrophobic plastic AM parts. Hizal *et al.* [21] was able to develop an aluminum material that was not only hydrophobic and also possessed a very low bacterial adhesivity. The method used for this experiment included electrodeposition and etching using a wide variety of cleaning chemicals, as well as the

development of nanopillars on the aluminum surface. Low bacterial adhesivity would be very extremely beneficial in the medical and food processing industry. Unfortunately, the chemical coating used to make the material superhydrophobic was Teflon, which can be hazardous in many environments where the low bacterial adhesivity would be otherwise helpful [7], [21].

Another notable concern with chemical treatments in addition to environmental concerns is that of durability. Superhydrophobic surfaces that are treated with chemicals and some nanomaterial treatments are only conducted at the surface level, which is highly susceptible to damage. Abrasion in these superhydrophobic coatings reveal hydrophilic surfaces, often etched, which would compromise the function of these parts [22]. This is particularly true for engineered pieces, as natural specimens are able to repair themselves through cell growth [22]. With this, it would be highly beneficial to have a material that is hydrophobic without surface treatments, which would only be possible by modifying the entire material instead of the surface. Modern chemical treatments do not possess this possibility, but additive manufacturing could make this more possible into the future and greatly increase relative superhydrophobic durability.

C. ADDITIVE MANUFACTURING IN HYDROPHOBICITY

1. Primary Advantages of Additive Manufacturing

3D printing is on the rise both commercially and industrially, and the reason is that AM provides numerous advantages compared to traditional manufacturing methods that will only continue to increase as the technology develops further. There is an incredibly large variety of AM methods ranging from binder jetting methods that can quickly produce large products to the fused filament fabrication (FFF) printers that are becoming more numerous for small plastic parts in offices and homes around the world. A majority of the focus in this report, however, will be on metal printing methods. The advantages of these AM methods are the most relevant for this study.

Metal AM processes include a wide variety of production advantages that could be extremely beneficial to achieving a superhydrophobic state in a metal. One important advantage in this process is that a wide variety of materials could be used. 316L stainless

steel was used in this study, but the AM process could be repeated using a large number of materials to satisfy the necessary properties of a part [13]. If the properties and melting dynamics allow a material to be deposited by the nozzle or hopper and fused by a laser during the printing process, the material could be suitable for SLM AM. The other major advantage in additive manufacturing is that it allows many geometries unachievable in traditional manufacturing method to be feasible. Many AM systems are able to print at relatively high spatial resolutions compared to traditional manufacturing techniques, especially those that utilize a laser or electron beam to selectively melt material [13]. Given that superhydrophobicity is reliant on surface geometries that are at a microscopic scale or smaller, additive manufacturing could be a possible alternative to the chemical methods currently used. In addition, using AM does not require any additional specialization other than the ability to create a CAD model for the printer to read, which eliminates the need for further training. This one-size-fits-all solution would additionally eliminate the need for harmful chemical to be present to promote hydrophobicity.

When combined with a method of manipulating surface energy density and the implantation of nanomaterials, AM could have the potential to achieve superhydrophobicity. It has been shown that chemical composition alone on a smooth surface is unable to achieve a water contact angle above 120° using known materials [20], indicating that both chemical composition and geometry are essential. This idea does not change when working with additive manufacturing to achieve superhydrophobicity, but it could allow for a user to create their own superhydrophobic parts and prototypes if the correct properties are found in the building material. For example, in an AM approach, an entity would be able to generate or purchase a metal powder or filament that was doped with another material (e.g., nanomaterials). With particular coating geometries, this hydrophobic building material could produce a superhydrophobic part. The metal powder or printer filament could be transported anywhere in the world and can be highly repeatable in nature. The only consideration on the end-user would be the surface geometry and printing parameters, which could be packages and automated to reduce necessary training.

2. 3D-Metal Printing and Selective Laser Sintering

Selective laser melting is a method of additive manufacturing that may be used to produce small metal parts in an especially precise manner. The premise of selective laser melting is that a thin powder layer is spread across a building area and is then locally melted using a high intensity energy source. This powder is often randomly packed in a powder bed across the surface, where the powder is locally melted using the laser. This will cause a small amount of powder displacement on the bed as the metal is melted, as well as a small amount of powder to be ejected from the surface of the powder bed due to the power of the laser. Because of this, all methods of powder bed printing inherently have a limited resolution and risk of porosity within the sample. This is minor, however, as the resolution is primarily dictated by the spot size of the laser which is highly refined in most situations. The energy is directed to a very fine point, and subsequent melt pool dynamics are controlled through printing power and velocity. There are a variety of laser types that can be used in the printing process, including Yb-doped fiber lasers, Nd:YVO_4 lasers, and CO_2 gas based lasers. These different lasers each have their advantages and disadvantages, like choice of laser when working with different materials. Other considerations: how much power is necessary for the melting process and how compact the laser mechanism needs to be [13]. In addition to using lasers to selectively melt materials, some methods of additive manufacturing utilize a powerful electron beam which can operate using very fine resolutions, as low as 10–50 microns in some cases [13]. In a study conducted by Auburn University in 2022 [23], the printer used to print a stainless steel and carbon nanotube composite was a Concept Laser Mlab Cusing™ machine with a default laser energy density of 64 J/mm^3 using a 100W Yb: YAG fiber laser. Selective laser melting has a strategic advantage not only in its high resolution, but additionally in its ability to produce martensitic structures, and parts with higher strength at the cost of low ductility. A disadvantage of SLM printing is that the laser is generally unable to self-correct mistakes from previous powder layers. The laser is only able to effectively melt a few layers of powder at once. If an error occurs in the printing process that prevents complete fusion or improper porosity, this error is unlikely to be properly repaired in future layer and the defect

will likely be permanent. Another disadvantage of this AM processes the inability to produce hollow parts without entrapping unfused powder [13].

When using a SLM, one of the biggest considerations to be made is controlling the power and energy density of the laser beam. The energy density across the surface is determined primary through the energy density equation, as seen below.

$$ED = \frac{P}{VHW} \tag{4}$$

In Equation 4, P represents the power being given to the laser, V represents the velocity of the laser moving across the surface, H is the layer height of the powder being melting, and W represents the hatch spacing or width of the melt pool being formed. All materials must meet a certain energy density threshold in order to melt, and many of these parameters guide the melting dynamics of the material during printing. It is important to find the proper combination of power and velocity when printing to fully melt the powder to allow for part formation immediately prior to re-solidification, but not so much energy so that the melt pool formed by the laser melts significantly deeper than the few layers necessary for proper formation. When the power is very high and the velocity is low, this effect is known as keyholing which can negatively impact the printed structure. If the power is very low and/or the velocity is too high, the melting may be insufficient to form its proper shape or the layers of powder will not fully fuse together in the print [13]. This balance of variables is shown in greater detail in the chart found in Figure 12.

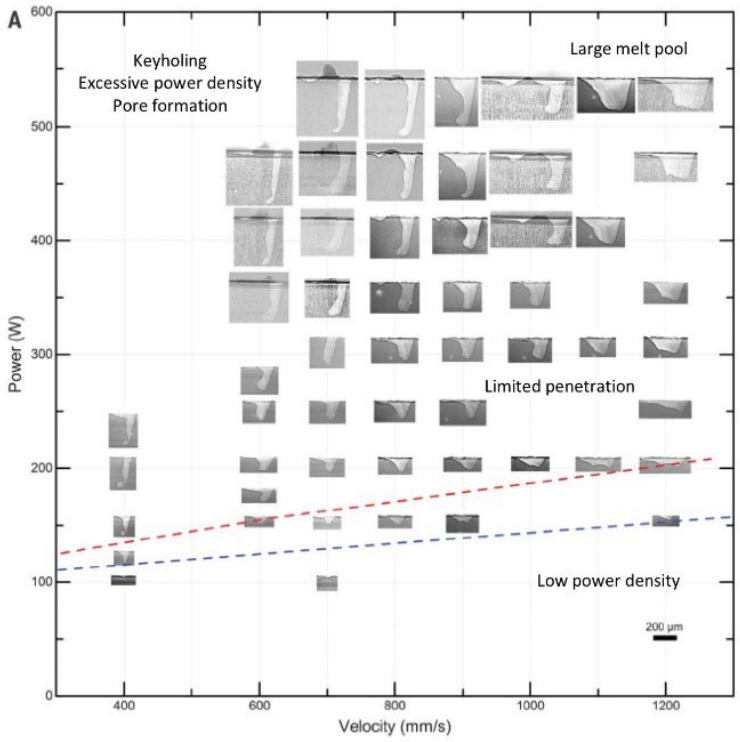

Figure 12. Energy density variable balance. Source: [13].

3. Hydrophobic 3D Printed Materials

In 2014, a study was conducted by Milionis *et al.* [20], looking to achieve superhydrophobicity in several 3D printed plastic parts using a dip coating process after printing. This study used two different methods of coating to achieve superhydrophobic results in ABS plastic, a common filament for FFF printers. The process consisted first of sputter coating a 20nm layer of Au/Pd to the surface of the material, followed by dip coating the plastic in a solution of acrylic fluoropolymers and hydrophobically modified fumed silica. The second approach relied on the same finishing layer, but a dip coating of superhydrophobic rubber was applied rather than sputter coating.

In a comparable approach to this study, Kaur *et al.* [24] was able to develop a method of directly producing superhydrophobic materials through a different process of AM known as digital light processing. This study was able to utilize a hydrophobic polymer base that was cured into the desired part shape via digital lithography. This form of AM is reliant on a specific form of material that can be cured with digital light lithography, which

is not applicable to any current metal materials known. However, this study engineered a hydrophobic material without the use to post-processing chemicals and coatings, aligning with the goal of this thesis.

D. NANOMATERIALS IN HYDROPHOBICITY

1. The Role of Nanomaterials in Hydrophobicity

Nanomaterials are defined as any material in which a dimension of its volume is measured in the nanoscopic scale (1–999nm). Nanomaterials often result in a significantly high surface area to volume ratio, which allows for some unique properties that may vary from the bulk properties of the same material. As an example, the melting point of gold, which is often considered a constant property of the metal, varies at nanoscopic levels. When gold particles are smaller than 5nm, melting occurs at lower temperatures [25].

Melting point is not the only material property that changes as samples move to the nanoscopic scale. Specific heat capacity, thermal conductivity, chemical properties, and wettability all are affected by the size of particles. In a review conducted by Ahmed *et al.* [26], several variations of nanomaterials were incorporated into different molten salts, paraffins, and other heat transfer fluids to modify the thermal conductivity and heat capacity of such fluids in a manner advantageous to heat transfer and energy storage. One of the most common approaches to modifying wettability is the implementation of nanomaterials on the surface of a substrate [27]–[30]. These processes are used primarily to achieve roughness in a stable form along a substrate, but still require a degree of chemical treatment or alteration to successfully develop a superhydrophobic surface. Some nanomaterials, however, are able to create a superhydrophobic surface based on the array distribution, already possessing desirable surface tension properties [31]. Nanomaterials have potential in developing superhydrophobicity as an alternative to surface energy modifications and roughening methods that could otherwise involve environmentally harmful chemicals or sophisticated instruments.

2. Carbon Nanotubes

For this thesis, carbon nanotubes will be used. These structures are often fabricated at a diameter in the tens of nanometers with lengths ranging from the nanometer to micron scale, as long as 100 microns [31]. Carbon nanotubes are well known for their ability to improve conductivity in composites and their outstanding mechanical properties, as well as other unique surface property modifications. These nanomaterials are used due to their milling compatibility with 316L stainless steel (SS) and evidence to ideal surface wettability properties. An example of these properties can be found in an experiment conducted by Wang *et al.* [31]. The authors explored the wettability performance of carbon nanotubes places in a 316L SS pillar array with varying porosities and spaces in between the pillars. The results of these experiments show a superhydrophobic static contact angle of over 160 degrees with low porosity, and a hydrophobic behavior at higher porosity of around 140 degrees. This experiment was conducted with a large majority of carbon nanotubes oriented normal to the substates, which would not be readily achievable in an SLM AM environment. An important consideration for this experiment is that there was no chemical coating applied in this experiment. The chemical composition of the carbon nanotubes themselves possessed a surface energy conducive to hydrophobicity, which is likely why the lower porosity sample aligning a greater perceived roughness was able to achieve superhydrophobic conditions.

The stainless steel being used in this experiment already has higher than typical contact angles among its metal counterparts. When properly treated, laser based methods of roughening minor surface energy modification are able to achieve hydrophobic to superhydrophobic results [32]. With the goal of achieving hydrophobic chemical composition prior to taking any geometric form, the formation of stainless steel composites with carbon nanotubes could have potential for superhydrophobic surfaces as printed.

THIS PAGE INTENTIONALLY LEFT BLANK

III. EXPERIMENTAL METHODS

A. MODEL DEVELOPMENT: MODELLING OF HYDROPHOBIC SAMPLES

The EOS M100 SLM printer will be utilized under a variety of input geometries, printer settings, and powder material. Each of these characteristics guide the material properties of the sample and will be individually modified in this thesis to determine their effects on wettability.

As previously discussed, the geometry and surface energy of a sample play the greatest role in overall wettability and hydrophobicity. Thus, a starting point in developing a superhydrophobic sample is generating a CAD model optimized with the governing equations for wettability (1)(2)(3) in mind. It is important that the models' dimensions still conform to the limits of the printer. In the case of the SLM printer being used, the goal is to optimize the real to projected surface area ratios and potential air gaps while still conforming to the approximate 100-micron resolution limit of the printer. Many of the CAD-based models used in this experiment were developed initially through Autodesk Tinkercad®, and all models were redeveloped using Dassault Systèmes SolidWorks® for simplified alterations and file compatibility. Several models were created in this experiment to optimize hydrophobicity through geometry as well as allow for characterizing measurements.

a. Pillared Geometry Samples

The primary method used in this experiment to optimize results was the use of a pillar geometry (Figure 13). This pillared geometry was developed to imitate the cones seen in nature at the smallest scale reasonably achievable in the AM environment. Variable pillar heights were implemented to explore the significance of pillar height in developing air pockets.

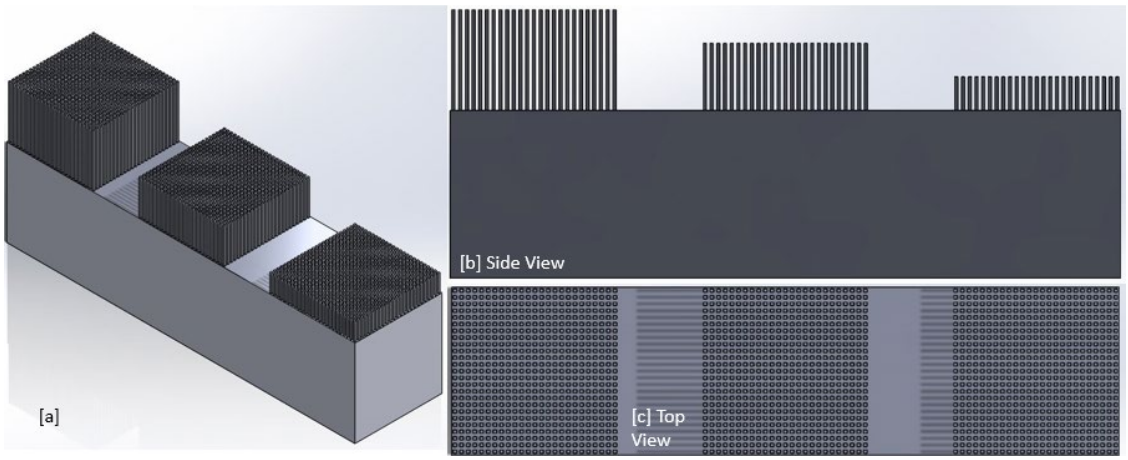

Figure 13. Orthographic view of pillared sample model (a), side view of pillared sample model (b), and top view of pillared sample model (c).

The geometry seen in Figure 13 is made up of a 20mm by 5mm by 5mm rectangular prism base with three different sets of pillars that each take up a 5mm by 5mm projected surface area. The model has these pillars set to a height of 3mm, 2mm, and 1mm from left to right. Each of these three projected surface areas consists of 625 microscopic pillars, each of which are 100 microns by 100 microns squares in an alternating pattern with 100-micron gaps in between each pillar. This value of 100 microns was the result of both the manufacturer published resolution limit as well as experimentation discussed further in this report.

b. Flat-Plate Geometry Samples

In addition to the pillared geometries outlined above, additional samples were generated to provide a control geometry for material characterization methods and ease of experimentation. In order to do so, two reference geometries were created, as outlined in Figure 14.

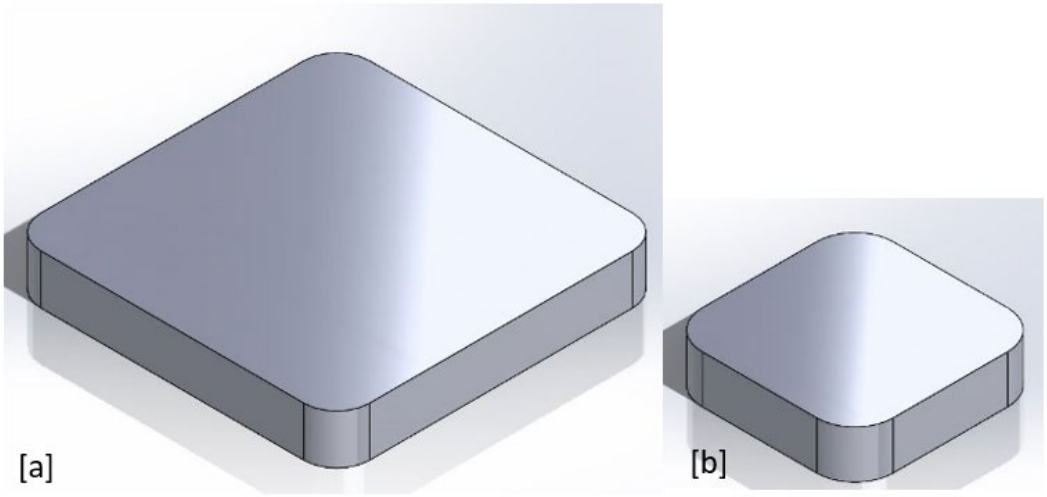

Figure 14. SolidWorks® model of large flat plate (a), and SolidWorks® model of small flat plate (b)

These two rectangular plates were designed for this experiment due to their repeatability using a SLM printer, compatibility with the Krüss Mobile Surface Analyzer (MSA) intended to collect water droplet data, and smaller sample size that allows for future microstructure analysis. The model had a ~2mm height, and surface area was approximately 10mm by 10mm for the small squares and 20mm by 20mm for the large square samples. All flat plate models were finished with a 1mm fillet on each corner since the printing method used is generally more accurate with curved portions than sharp edges.

c. Unique Geometry Samples

In an effort to explore further hydrophobic geometries, several additional geometries were modeled to optimize roughness. Three alternative geometries were explored. The first unique geometry developed, seen on the Figure 15[a], attempts to create a small square sample with a matrix of 100-micron cubic pillars. This geometry is most comparable to Figure 13, but the pillar height was reduced to 100 microns to optimize the simulated roughness and further explore the variation of pillar height. This reduction in pilar height likely will not give room for an air pocket underneath the sample. The drawback could, however, come at the advantage of minimizing the potential for mechanical issues such as bending or buckling.

The second unique geometry presented in Figure 15[b] is a reversal of the previous sample. To do so, the 100-micron previous extrusion of the pillars was replaced with a 100 micron extruded cut into the main body of the sample. The reason for exploring this geometry was to observe the effects of replacing one large and interconnected potential air pocket with a multitude of individual microscopic air pockets. These two unique geometries were combined in a checkerboard-style pattern in order to produce a third unique geometry that can be seen in Figure 15[c]. This model was generated in the attempt to optimize the true surface area in comparison to the project surface area.

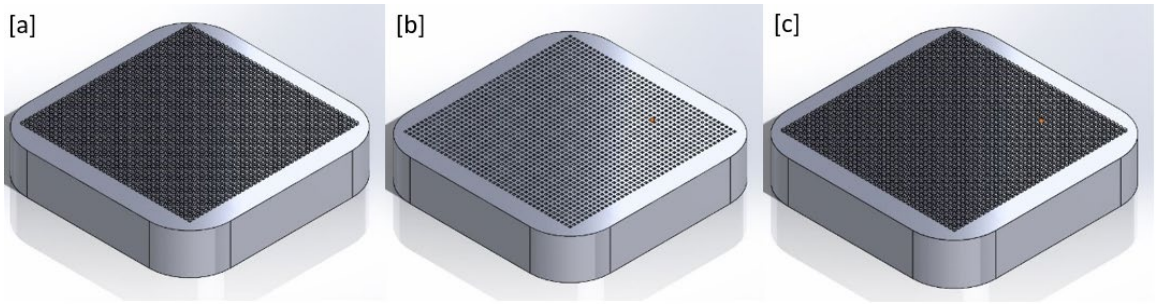

Figure 15. Flat plate sample with 100µm cubic pillar surface finish (a), flat plate sample with 100µm cubic indentations on surface (b), and flat plate sample with alternating 100µm cubic pillar and indentations along surface (c)

B. BALL MILLING PROCESS

In order to incorporate nanomaterials into the SS powders, the CNTs were milled into the stainless steel powder utilizing the SPEX sample prep high energy ball mill (HEBM) seen in Figure 16. The parameters used to conduct this testing are outlined in Table 2. All percentages used in this table reflect volumetric percentage. In calculations, the density of 316L stainless steel was determined to be 8.0 g/cm^3 [33] and 2.1 g/cm^3 for the CNTs [34].

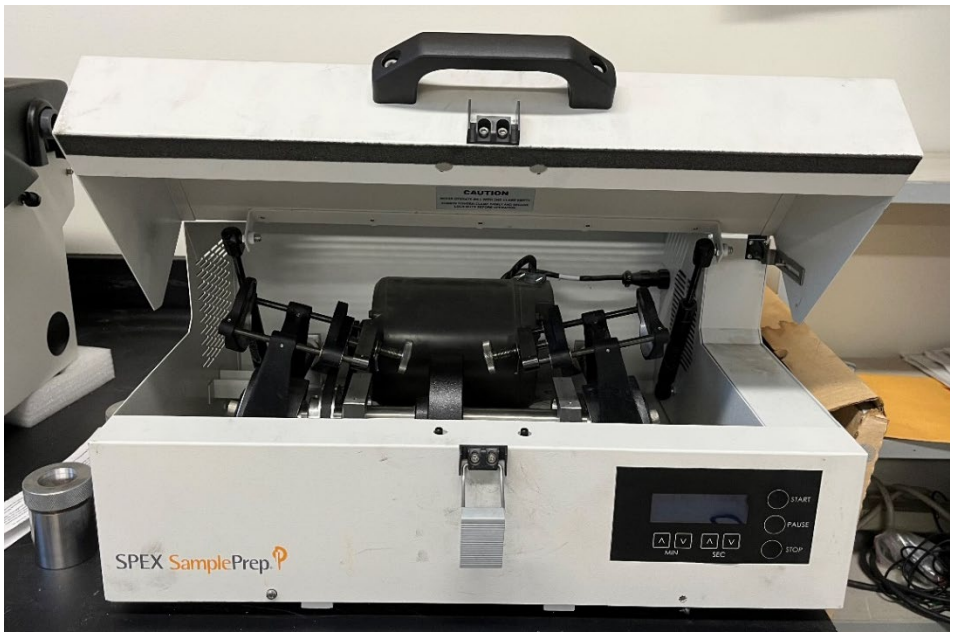

Figure 16. SPEX sample prep high energy ball milling machine

Table 1. Ball milling parameters for powder preparation

Powder	Time On	Time Off	Cycles	Ball:Powder Ratio (BPR)	Mass of SS in canister	Mass of MWNT
1%-CNT SS	5 minutes	5 minutes	5 cycles	1:2	75 g	0.197 g
2%-CNT SS	5 minutes	5 minutes	10 cycles	1:2	75 g	0.394 g
5%-CNT SS	5 minutes	5 minutes	15 cycles	1:2	150 g	1.969 g

Two iterations of 5% CNT powder, with differing powder-to-ball ratios, were produced due to an overly aggressive milling process. The second iteration of 5% CNT powder underwent 15 cycles due to large amounts of residual carbon not being distributed into the powder after 10 cycles, as evident in the image in Figure 17. Residual carbon results were comparable after 15 cycles, but the powder was still sent forward for further characterization at this point.

Figure 17. Residual carbon in 5% CNT milling process

C. EOS M100 3D PRINTING PROCESS

1. Software Setup

a. Generation of Support Structures

The SLM additive manufacturing process is most often a procedure that requires post-processing to successfully generate a print. In order to simplify sample removal, support structures must be used. Support structures are also necessary for building parts with overhangs or complex geometries that require additional building support. The Materialise Magics program was used in this experiment to organize parts on the build plate, generate support structures, and convert all CAD files into a file that can be read by the EOS printing program. All samples containing the same concentration of carbon nanotubes were printed on the same build plate when possible, to reduce printing time. In the example shown in Figure 18, three small plates, three large plates, and a pillared sample were generated on a single plate. This corresponds to the necessary samples to test three different laser energy densities in a single printing iteration. The orientation of the samples within the build plate was designated to isolate each set of energy densities to a single line. This was done in case of part failure resulting from improper melting dynamics, which would only impact the successful printing of parts of the same failed energy density.

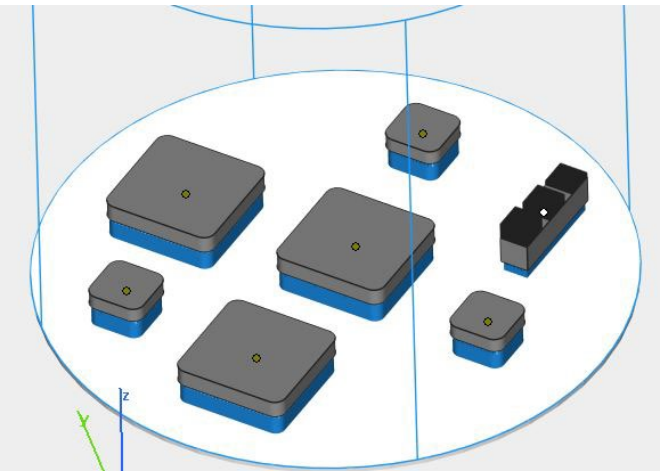

Figure 18. Materialise Magics printing software

Once properly oriented, default support structures approximately 1 to 1.5mm high were added to each sample, seen in blue in Figure 18. Since the default support structures could be insufficient in supporting the corners of some parts, a cone support was placed at all four corners of each sample to ensure that no drooping occurs at the corners when the parts are being built.

b. Laser Energy Density Modifications

The energy density was found to be approximately 67 J/mm^3 under the default settings of the printer when calibrated to print using 316L stainless steel powder. In addition to the utilized default settings, the laser energy densities of 60 J/mm^3 and 80 J/mm^3 were generated for the experiment. These values were chosen since they were close to the default printer settings, slightly higher and lower than the default settings, and the settings which were previously utilized under Jalagam Prajna. The parameters which were modified to create different energy densities is outlined in Table 2. All pillared samples were printed using only the default energy density settings of 67 J/mm^3.

Table 2. Laser energy density variables

Energy Density [Units: J/mm^3]	Power (W)	Speed (mm/s)	Hatch Spacing (mm)	Thickness (mm)
67 (Default)	77.1	827	0.07	0.02
60	77.1	917	0.07	0.02
80	76.8	800	0.06	0.02

These values correspond to both the stripes and upskin parameter settings of the EOS software suite. The downskin settings were left unmodified, as previous modification was found to lead to print failure. Upon creating each of these energy density settings, each part was assigned an energy density configuration and uploaded to the 3D printer.

2. Physical Printer Setup

The printer used for this experiment was the EOS M100 SLM printer, seen in Figure 19. A stainless steel build plate was placed onto the stage. Upon conducting a thorough sifting of all powder, particularly previously used powder, the powder was placed into the hopper. Prior to starting the printing process, an initial layer of powder was used to coat the build plate as seen in Figure 21 and the building chamber was filled with argon gas. In order for the printer to properly operate, the partial pressure of oxygen must be lower than 0.15% within the chamber. This prevents the possibility of powder oxidizing at the high temperatures of the printing process and negatively impacting bonding.

Figure 19. EOS M100 SLM printer

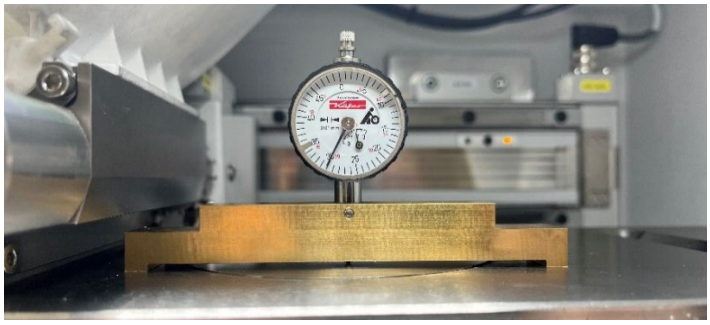

Figure 20. Setting the build plate to 30 microns

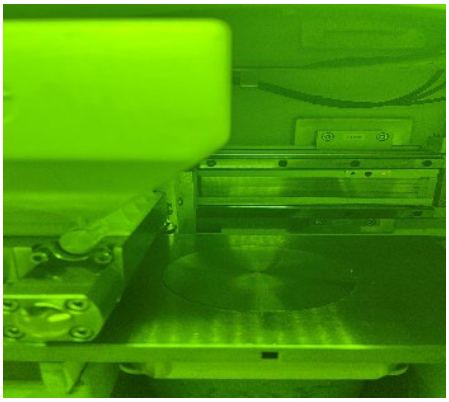

Figure 21. Conducting initial recoating of 5 vol. % CNT print

D. MATERIALS CHARACTERIZATION PROCESS

1. Scanning Electron Microscopy

In order to obtain high resolution images of samples, a scanning electron microscope (SEM) was used. For a majority of the images procured, the Zeiss NEON 40 SEM shown in Figure 22 was used. A SEM does not magnify light as a normal microscope, but rather focuses an electron beam onto a surface and detects the resultant backscattered and secondary electrons emanating from the sample. Since an electron beam has shorter wavelengths and a smaller energy spread (i.e., smaller wavelength spread) compared to light, this form of microscopy can allow a user to see at otherwise unfeasible scales. This sort of imagery was used for the characterization of the building powder, as well as the printed samples to identify any characteristics that would not be otherwise visible to the human eye.

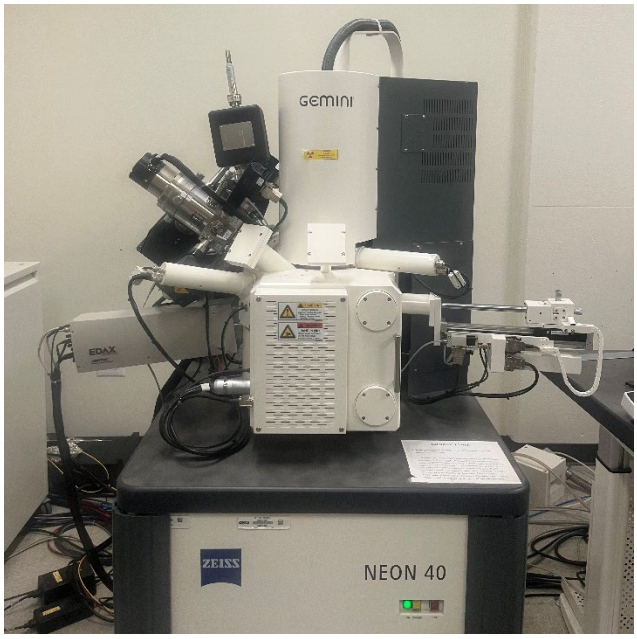

Figure 22. Zeiss scanning electron microscope

In addition to the Zeiss SEM outlined in Figure 22, the Thermo-Fisher Scientific (FEI) Inspect f50 SEM was used. These two microscopes operate under the same principles and would produce virtually identical results if operating under the same conditions.

2. Krüss MSA Water Droplet Analysis

A Krüss mobile surface analyzer (MSA) was used for measuring contact angles. This instrument, seen in Figure 23, consists of two magnetic nozzles attached to syringes of water and diiodomethane. The reason that diiodomethane is used in the MSA system is due to its well-known surface tension properties as a non-polar fluid with similar surface tension to water [35]. When instructed, the system delivers a sessile droplet from either or both of the nozzles at a size input by the user ranging from 2 to 20 microliters. Following the drop distribution, the instrument then takes an image of the droplets resting on the surface and uses an image analysis software to show and record the contact angles. An example of one of these measurements may be seen in Figure 24.

Figure 23. Kruss mobile surface analyzer

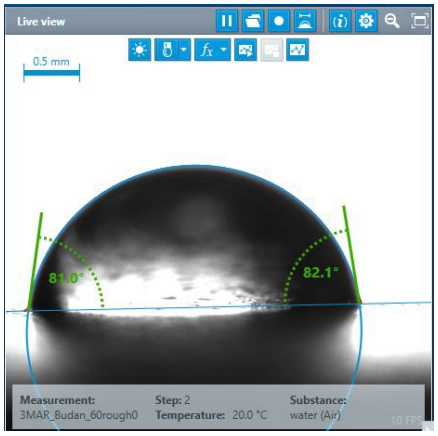

Figure 24. Kruss MSA contact angle measurement of pure stainless steel with a milled surface finish

Due to a malfunction of the nozzle system in the Kruss MSA and the inability to take accurate measurements of the pillared samples with various heights, other methods were used to conduct contact angle measurements with the samples. For all samples, a Fisherbrand micropipette, as seen in Figure 25, was set to 2 microliters and used to create water droplets on the samples. An attempt was made to drop all droplets from an identical height of 1mm, but this was difficult to obtain due to water droplets often remaining attached to the micropipette until coming into contact with the sample. In order to obtain contact angle measurements of these droplets on flat plates, the Kruss MSA system was used to take an image of the droplets. Upon creating the drop, the MSA was quickly placed on top of the sample and aligned to take an image, as the measurement was meant to be within a second of the drop. This time between conducting a drop and measurement was often longer than one second, which could generate measurement error in this experiment. For measuring the pillared samples when using the MSA was not possible, a 4K resolution video was taken of the drop distribution and later analyzed using ImageJ photo analysis software. The setup used to create these videos consisted of a platform to keep the camera stationary and level with the water droplet, and sufficient tape to keep all items stationary without interfering with the experiment. All samples were sufficiently dried between measurements and stored in a vacuum chamber to prevent corrosion or adverse reactions over the course of the thesis.

Figure 25. Fisherbrand elite micro-pipette

3. Optical Profilometer Analysis

In order to obtain roughness measurements of the flat plates, a Zygo optical profilometer was used inside a class 10,000 clean room. This system, pictured in Figure 26, operates under the principles of focused light. Upon obtaining a focused image of the sample, an estimate of how much variation in height is calculated. The instrument changes

the focus of the light from the projected high point of the sample to the projected low point of the sample, recording all segments of the image that appear to be in focus at a given height. These results are then compiled into a topographical map of the surface where the range and deviation in roughness can be established analytically.

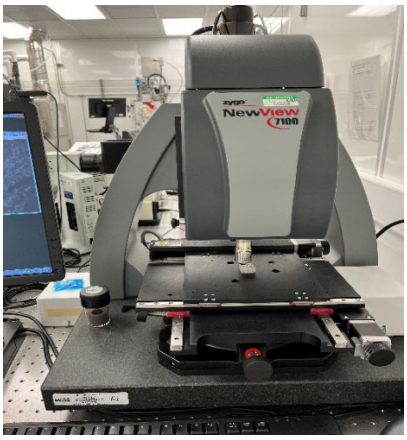

Figure 26. Zygo optical profilometer

E. EOS M100 3D PRINTER RESOLUTION TESTING

In order to further increase surface area within the given volume and better mimic the superhydrophobicity that occurs naturally, models with a finer resolution than the manufacturer's suggested limit were created. This would create a larger surface area than previously achievable, which would have the possibility of improving hydrophobicity. This was done using two separate procedures.

The first experiment performed to increase the resolution of the model was done using nearly identical models to those presented in Figure 13. The fundamental difference between Figure 13 and the other samples of this procedures was the size of the pillars and spacing in between them. Figure 27 demonstrates the three different models utilized in this experiment. Figure27[a] is identical to that of Figure 13 with 100-micron pillars and 100-micron gaps in between each pillar. Figure 27[b] has a pillar size of 75 microns with a gap of 75 microns in between each pillar. Figure 27[c] is based on a 50-micron pillar size and gap. This procedure was doing using 316L stainless steel powder and a laser energy density setting of 67 J/m^3.

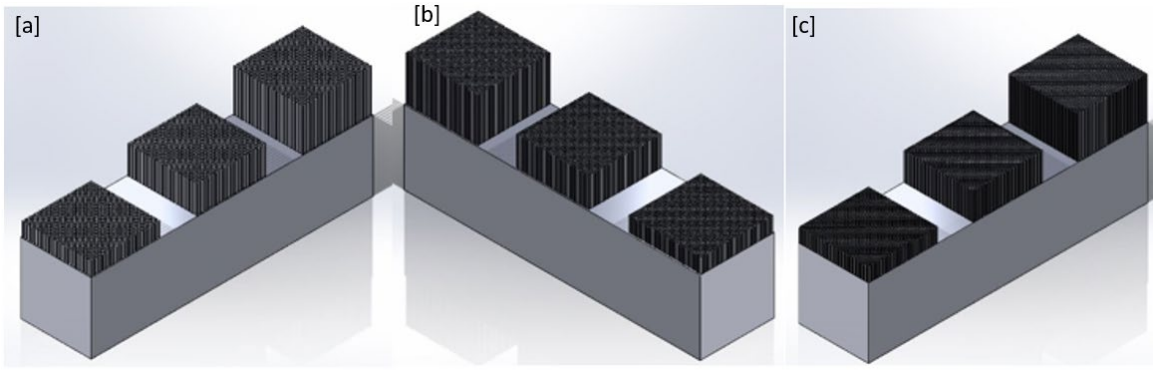

Figure 27. 100µm pillared sample (a), 75µm pillared sample (b), and 50µm pillared sample (c)

Based upon the results of the first procedure, a second procedure was developed in an attempt to produce a refined geometry through the use of a cone structure. Cones were chosen because they were rounded, which caters to how the printer operates at higher resolution. Another advantage is that cones gradually decrease in size in a manner that will provide the possibility to see the absolute resolution limit of the printer using default laser parameters. When building these conical geometries seen in Figure 28, three different starting base sizes were explored. The left cluster of cones had a base size of 150 microns, and the right cluster of cones had a base size of 200 microns. The center cone is the largest with a base size of 500 microns. The goal of this experiment was to determine the smallest resolution achievable with default laser settings.

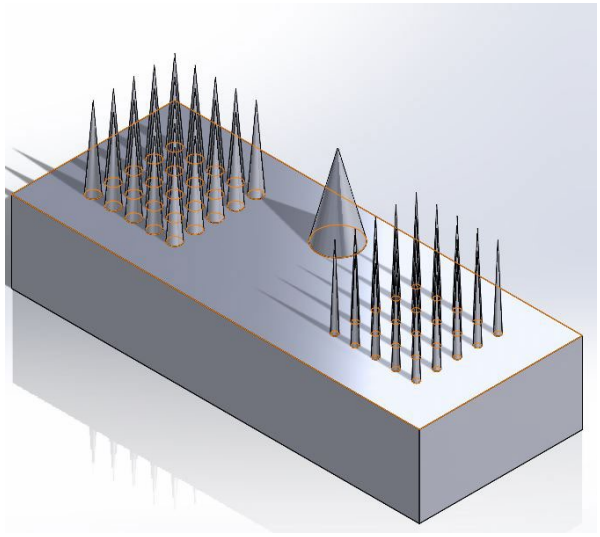

Figure 28. Cone geometry test

IV. FLAT PLATE WETTABILITY CHARACTERIZATION

In this chapter, the effects of laser energy density modification and carbon nanotube composition on surface wettability will be explored.

A. MICROSCOPY OF MILLED 316L STAINLESS STEEL POWDER WITH CARBON NANOTUBES

SEM Micrographs were taken of the stainless steel printing powders with 0% (pure), 1%, 2%, and 5 vol. % CNT. The images seen in Figure 29 show both 0% and 1 vol. % powders, comparing the presence of carbon nanotubes. These images show the presence of carbon nanotubes based upon the large variation in images between Figure 29[a] and Figure 29[b]. Images in Figure 29[a,b] are taken at the same scale for comparison. Individual carbon nanotubes are indicated in Figure 29[b] by the large white line in the figure, as well as the several smaller white lines indicative of partial CNTs. The individual carbon nanotubes found in Figure 29[b] indicates HEBM mixes the powder without damage to the CNTs. Figures 30–33 indicate non-homogeneous mixing is also present in the powders used in this thesis, evidence of individual nanotubes shows that HEBM is sufficient for creating these composite powders.

When observing the contrast between samples in Figures 30 [a] through [d], one can see that the carbon nanotubes have the tendency to stay together in the milling progress. The dark spots found in the powders in Figures 30 [b] through [d] correspond to clumps of carbon nanotubes that were not evenly mixed throughout the process. It is desired to keep this clumping to a minimum, as excessive clumping could generate a variety of printing issues. Many of these issues are based on the ability of the powder to be successfully fed though the hopper and the relative viscosity of the printing material. Qualitative data shows that material with a higher volumetric percentage of CNTs is susceptible to stick together when stagnant in a container or the printing hopper. This is comparable to the effects of water on sand. The most likely reason for this sticking is because clustering of CNTs act in a similar nature to adhesives and allow particles to stick. CNT clumping found in Figure 30 indicates that CNTs prefer to adhere to other CNTs as well as the SS particles. Images

indicate that groupings of carbon nanotubes can act as a binder between particles in a similar manner to what is seen in Figure 31, and the probability of these binding occurrences increases with CNT concentration.

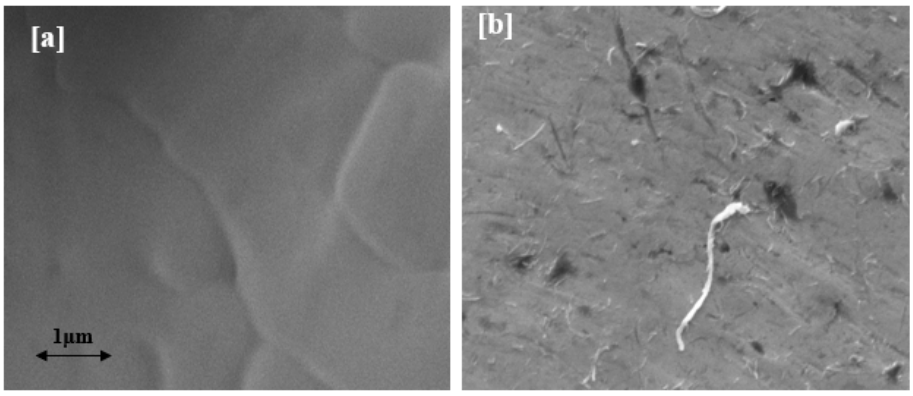

Figure 29. Pure 316L stainless steel powder as-received (a) and 316L stainless steel powder composite with 1 vol. % CNT, mixed through HEBM (b)

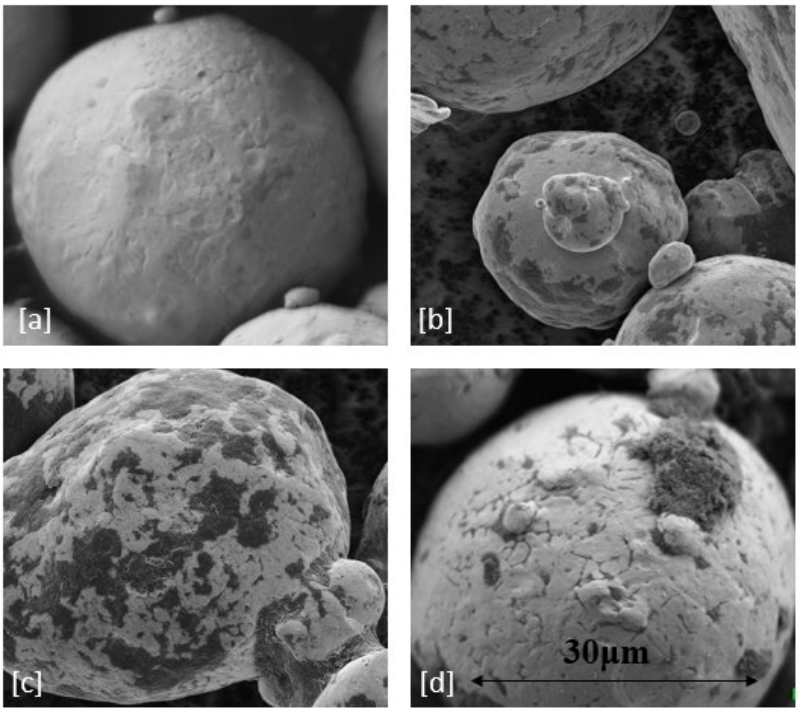

Figure 30. Pure 316L stainless steel powder particle (a), 316L stainless steel powder composite particle with 1 vol. % CNT (b), 316L stainless steel powder composite particle with 2 vol. % CNT (c), and 316L stainless steel powder composite particle with 5 vol. % CNT (d)

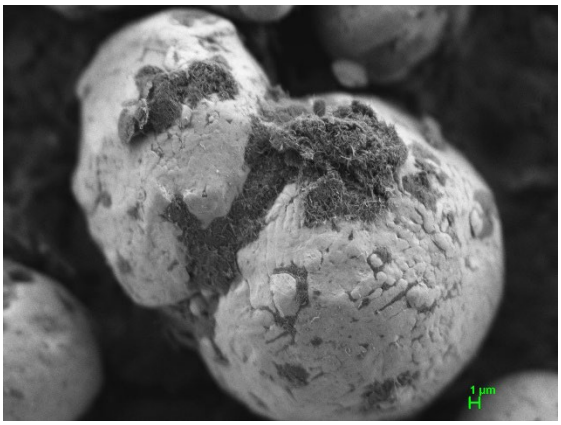

Figure 31. Two particles stuck together with CNTs in the 5 vol. % carbon nanotube stainless steel composite powder

Figure 32 shows different CNT concentrations of SS composite powders. The green circle in Figure 32[a] is 25µm in diameter, the approximate size of individual particles. It is estimated that particles range in size from near 8µm to over 30µm. Since all particles are sufficiently below the printing resolution, this sizing would be unlikely to affect printing resolution in the case of this thesis. Nearly every stainless-steel particle in Figure 32 [b] through [d] shows evidence of CNT clumping in the same manner as previously seen in Figure 30 [b] through [d]. When excessive loose CNTs were discovered within the powder upon completion of milling, particularly with the 5 vol. % concentration powder, there is a possibility of CNT saturation. This would be expected to be evident in microscopy though loose CNTs in the sample but is difficult to identify due to the background. However, observations such as those found in Figure 17 support that the amount of CNT added in the 5% sample is beyond the saturation limit for the particular milling process. Previous studies [23] show that the saturation point seen in this thesis is not based primarily on the material properties, but rather the method used for milling. Further milling could be done in attempt to overcome this saturation, but was not attempted to avoid any powder deformation, damage to CNTs, and time constraints associated with the process.

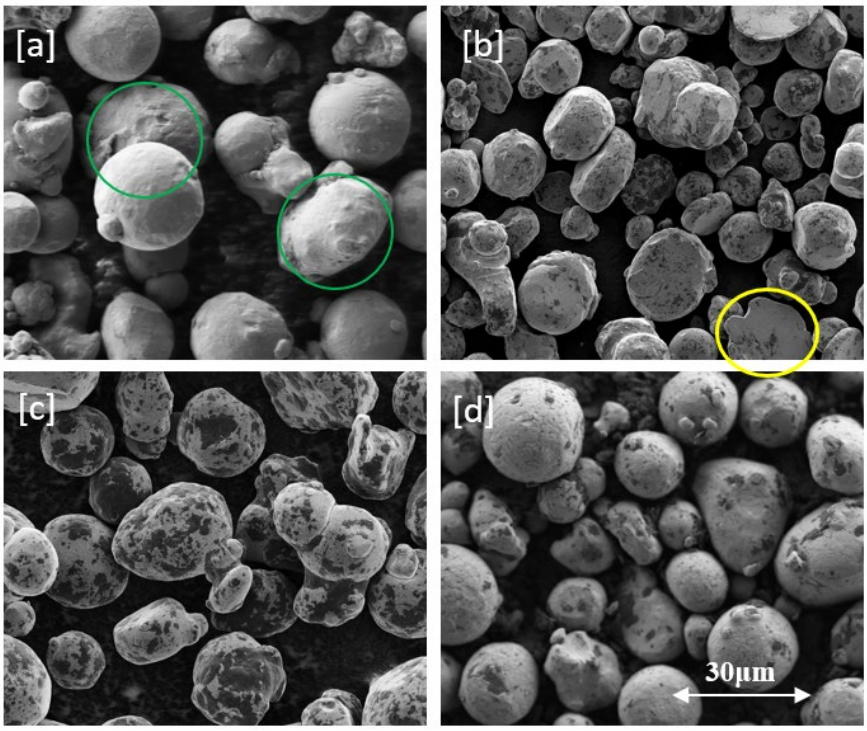

Figure 32. Pure 316L stainless steel powder particles with 25µm circle representing average particle size (a), 316L SS composite powder with 1 vol. % CNT and evidence of HEBM particle damage (b), 316L SS composite powder with 2 vol. % CNT (c), and 316L SS composite powder with 5 vol. % (d)

An additional phenomenon, which can be seen in Figure 33, is the deformation of powder particles as a result of the milling process. Low BPR and sufficient brakes in the HEBM process were used to prevent particle deformations and corresponding CNT destruction in the powder. Unfortunately, this damage is not completely avoidable while still sufficiently milling the powder. An example of particle deformation can be seen in Figure 32[b] (yellow circle) where a particle has been flattened. These deformations are not seen in the pure stainless-steel samples in Figure 32[a], as the powder did not undergo milling prior to imaging.. When a particle is damaged and flattened, it will take a disk like shape as opposed to the desired spherical shape. To visualize this, a sample milled at a 1:2 BPR is compared to a sample milled at a 2:1 BPR in Figure 33.

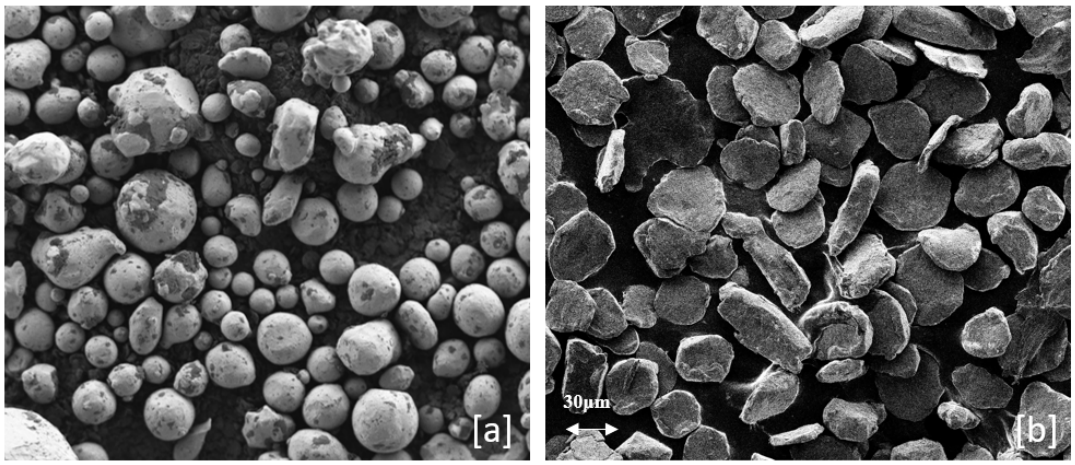

Figure 33. 316L SS composite powder with 5 vol. % CNT, milled for 15 cycles with a 1:2 BPR (a), and 316L SS composite powder with 5 vol. % CNT, milled for 10 cycles with a 2:1 BPR showing evidence of deformation and overmilling (b)

As Figure 33 shows, milling a ball to powder ratio greater than 1 can severely deform powder. Over-milling not only results in particle deformation, but severe destruction of CNT milled with the powders. Despite CNT being milled into the powder in Figure 33[b], there was no evidence of carbon nanotubes in the microscopy. All of the CNT pillars were subject to high impact from an excess of milling balls, which led to the CNTs breaking rather than mixing. These issues would be likely to cause issue when conducting prints on the SLM 3D printer, but this was not the case for the sample imaged above. Samples were able to successfully print at the same resolutions are pure stainless steel despite deformation.

The EOS M100 printer has shown to be resilient to a wide variety of stainless steel powders, successfully printing with 2 vol. % CNT in stainless steel as well as the highly deformed powder seen in Figure 33[b]. Future tests will be performed to determine if this powder can be used for successful printing and further characterization of the wettability results for this material.

B. SESSILE DROP CONTACT ANGLE MEASUREMENTS

Upon completing all prints, several sessile water droplet measurements were recorded using the Krüss MSA mobile surface analyzer. Several examples of these measurements can be seen in Figure 34. All of the measurements were combined to form the box and whisker plot shown in Figure 35.

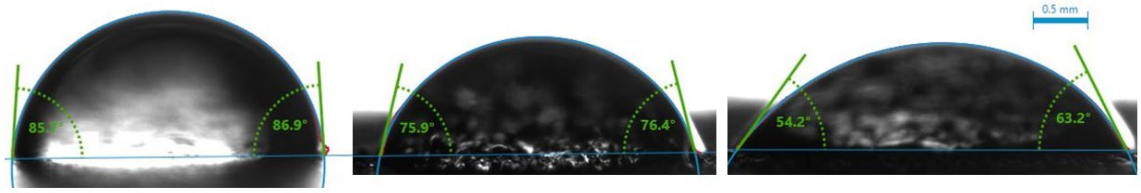

Figure 34. MSA contact angle images from pure stainless steel sample (milled), 2 vol. % CNT composite sample (ED60), and 1 vol. % CNT composite sample (ED80)

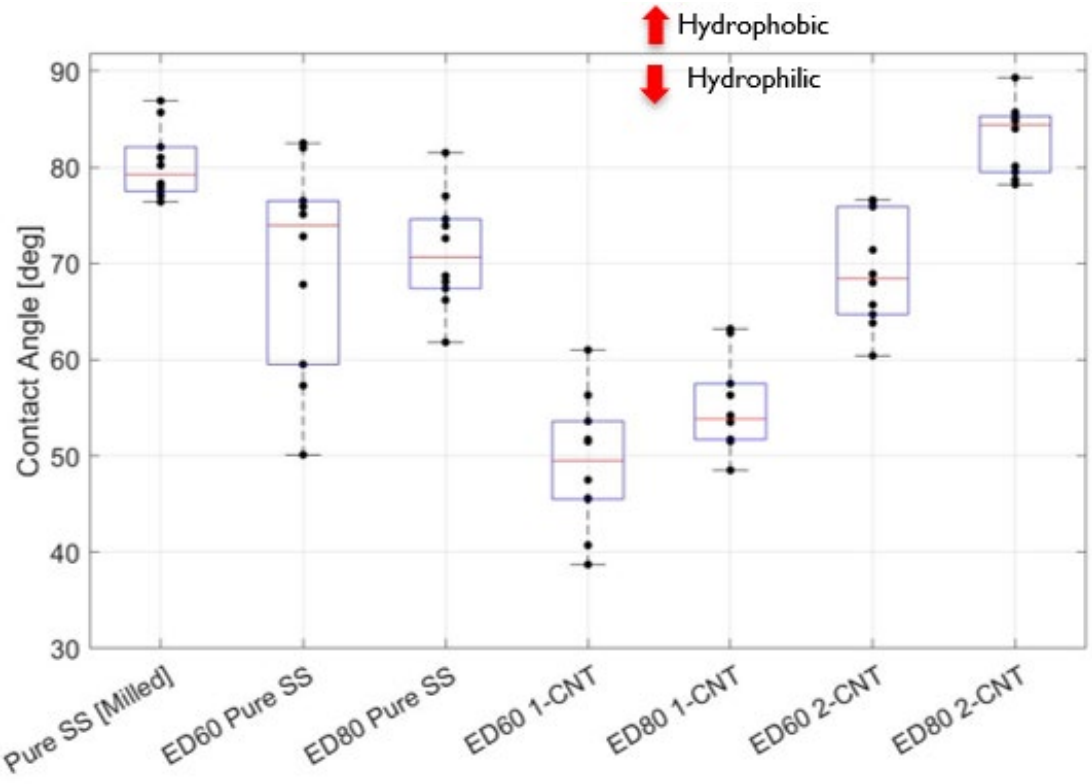

Figure 35. Measured contact angles for all SS composite samples

All data points in Figure 35 correspond to an image comparable to those found in Figure 34, and these data may be found in the supplemental data section in the Appendix of this report.

The plot found in Figure 35 shows several trends corresponding to both energy density and CNT concentration. With regard to CNT concentration, it is difficult to form a trend based on the resultant data. The highest concentration of CNTs performed at the highest contact angle of all sample, but these optimal results only appear in a higher energy density. For the lower density, the performance was similar to the pure stainless steel on most droplets. Additionally, the stainless steel with a 1 vol. % concentration of CNT consistently had lower contact angles than other samples. This could be the result of a high variation in roughness, but future data shows that this is not the case. There are many possibilities that could warrant this unexpected trend such as nanostructure at the surface and porosity, or a unique trend in wettability for stainless steel composites under various CNT concentrations. This could be due to printing abnormalities that occurred during the printing process of the 1 vol. % CNT parts, as the tests were not conducted on samples with the same concentration from multiple prints as well. This data does not support a linear trend between CNT concentration and wettability, as the 1 vol. % composite had higher wettability than the pure stainless steel and the 2 vol. % composite had lower wettability. This does show potential in achieving hydrophobicity in future stainless steel composites, however. It would be anticipated that samples formed from 5 vol. % CNT powder would more closely resemble and further amplify any variation that exists between the pure stainless steel and 2 vol. % CNT composite. Since the 2 vol. % sample already performs within 5–10° of 90°, further increasing carbon nanotube concentration could allow for hydrophobicity. Therefore, one should not rule out the possibility of using CNTs to produce superhydrophobic stainless steel without further testing.

When observing the effects of laser energy density on sample wettability, all else being equal, higher energy density corresponds to a higher contact angle in two of the three CNT concentrations. The exception to this case is with pure stainless steel, which the difference between contact angles is least significant. The reason for this phenomenon is likely due to the size of the melt pool produced by the laser when conducting the print. A

higher energy density would correspond to a larger melt pool, which extends the time in which the metal experiences the melting and cooling process. This additional time, however small, leads to a smoother surface finish on the sample. The Wentzel equation (eq. 2) supports that a smoother finish would increase the contact angle in hydrophilic materials such as these, which aligns with the trends shown in energy density. This additionally supports the high contact angle of the milled stainless steel sample in comparison to other 3D printed samples, as it has been machined to a smoother finish.

C. SURFACE ROUGHNESS MEASUREMENTS OF FLAT PLATE SAMPLES

Many of the statements and explanations found in the contact angle measurements can be confirmed and augmented through measuring the surface roughness of these flat plate samples. This data will be used to determine the effects of both energy density and CNT concentration on surface roughness and associated wettability. Figure 36 shows a typical roughness mapping performed using the optical profilometer. The results of these measurements include a topographical map of the surface relative to the subjective surface height, allowing for visual representation of the data. As one can see when comparing the data from a milled sample to that of the as-printed surfaces in Figure 36, there are areas of the amp in which no data is collected. This can be the result of two different causes. The first of which is that the scan height is less than that of the peak to valley measurement. This is unlikely for any of the samples included in this thesis based on the peak to valley measurements being sufficiently lower than that of the scanning range of 300 to 500 microns. The second possibility is insufficient light exposure, which is divided into two different forms. The first is improper brightness at the emitting source, as the desired light exposure can be input by the user. Operating at too high of brightness may cause some portions of the image to become overexposed and washed out, making to impossible to find the point of focus. If too low in brightness, there could be insufficient light to see the image to find the point of clarity and focus. Since the as-printed samples likely have jagged points and obscure surface geometries, there was not a single brightness that was able to characterize an entire sample area. In order to improve results, two scans were run and overlayed at both a high and low brightness to maximize the surface area characterized.

The other form of improper brightness, accounting for a majority of the data gaps seen in Figure 36, is due to jagged and obscure geometry. Since the as-printed surfaces appear rough and have no district geometric pattern for roughness, there are likely areas of the surface that are inaccessible by the scanning light to observe in focus. An attempt was made to resolve some of these data gaps through tilting the measuring surface to give the light a different angle of reflection, but this was unable to fully resolve the data gaps.

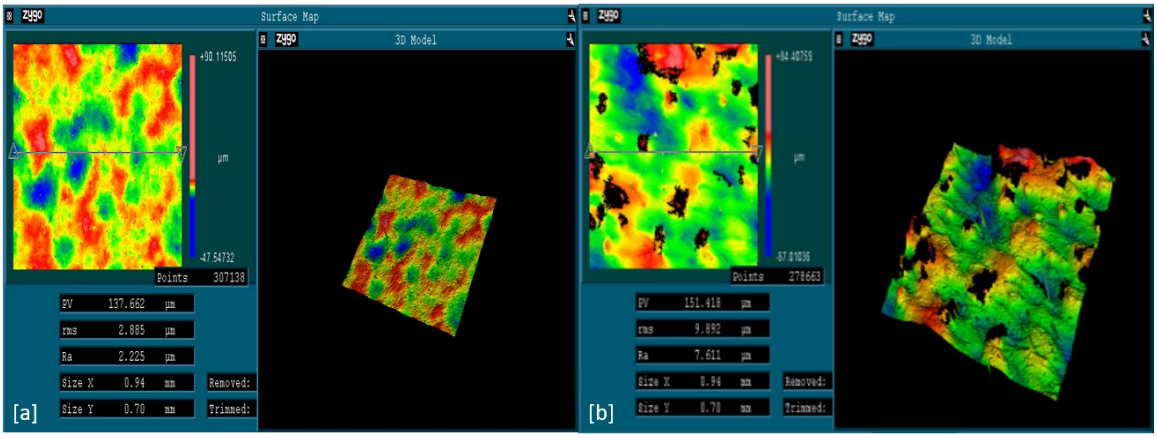

Figure 36. Optical profilometry map of milled SS sample (a) and optical profilometry map of 1 vol. % CNT SS sample (ED60) (b)

Despite these data gaps in many of the as-printed samples, the optical profilometry still provides valuable insight into the roughness of the sample. The data and topography of all samples collected can be seen in the supplemental data section in the Appendix of this report. In addition to the topographical maps seen in Figure 36, several statistical points are given for each measurement to quantify the roughness of the samples. The first data point is the peak to valley height of the sample, which quantifies the difference between the highest and lowest measured points for the sample. This gives insight into the occurrences of large peaks and valleys as well as assisting in determining the center height for future measurements. The second data point is the rms height for the dataset, which serves as a form of deviation in height throughout the sample. All summary of the data collected for optical profilometry can be seen in Figure 37.

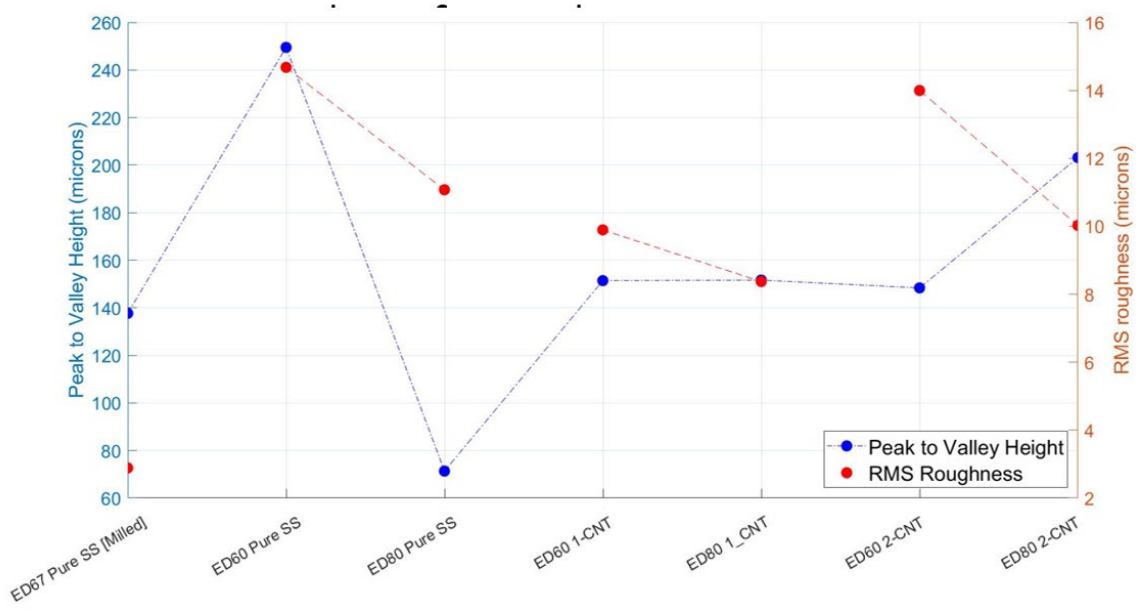

Figure 37. Roughness measurements for all SS composite samples

The peak to valley data seems to remain relatively constant at approximately 150 microns with the exception of low values for a single pure SS sample. The cause for the ED80 pure SS sample having lower than average values as well as the ED60 pure stainless steel sample having higher than average values is likely due to a presence or absence of major peaks in the small portion of the sample being analyzed. This is by chance and will not significantly dictate any roughness calculations since the topographical mappings for these samples are in agreement with the additional samples.

Trends in the RMS data are the best measured indicator of roughness based on the data available. The milled sample demonstrates an RMS value significantly lower than all other as-printed samples, which is expected. In each of the three CNT concentrations, a decrease in roughness was seen between the prints using a laser energy density of 60 and 80. The reason for this trend is the same as the trend in increasing contact angle previously discussed, which supports the claim that printer settings can have an impact on wettability through modification of surface roughness. In terms of concentrations, the pure stainless steel samples demonstrated the highest RMS roughness values. The 2 vol. % CNT SS samples also had high RMS roughness values comparable to the pure stainless steel. The

1vol. % CNT SS samples had the lowest RMS roughness values, which aligns with qualitative observations that the 1 vol. % CNT SS samples visually appeared smoothest.

D. DISCUSSION OF TRENDS BETWEEN ROUGHNESS AND DROPLET DATA

. A summary of the data collected through the sessile drop contact angle measurements and optical profilometry can be seen in Tables 3 and visually summarized in Figure 38. The effect on wettability due to the printer settings are discussed.

Table 3. Optical profilometry and contact angle measurements

Sample	RMS Roughness	Mean Contact Angle	Contact Angle Std. Dev.	Maximum Contact Angle
0%-CNT, Milled	2.885 µm	80.31°	3.647°	86.3°
0%-CNT, ED60	14.676 µm	69.95°	10.97°	82.5°
0%-CNT, ED80	11.072 µm	71.18°	5.814°	79.3°
1%-CNT, ED60	9.892 µm	49.21°	16.23°	58.7°
1%-CNT, ED80	8.372 µm	55.27°	4.782°	60.2°
2%-CNT, ED60	13.995 µm	69.18°	5.744°	76.2°
2%-CNT, ED80	10.024 µm	83.07°	3.698°	87.5°

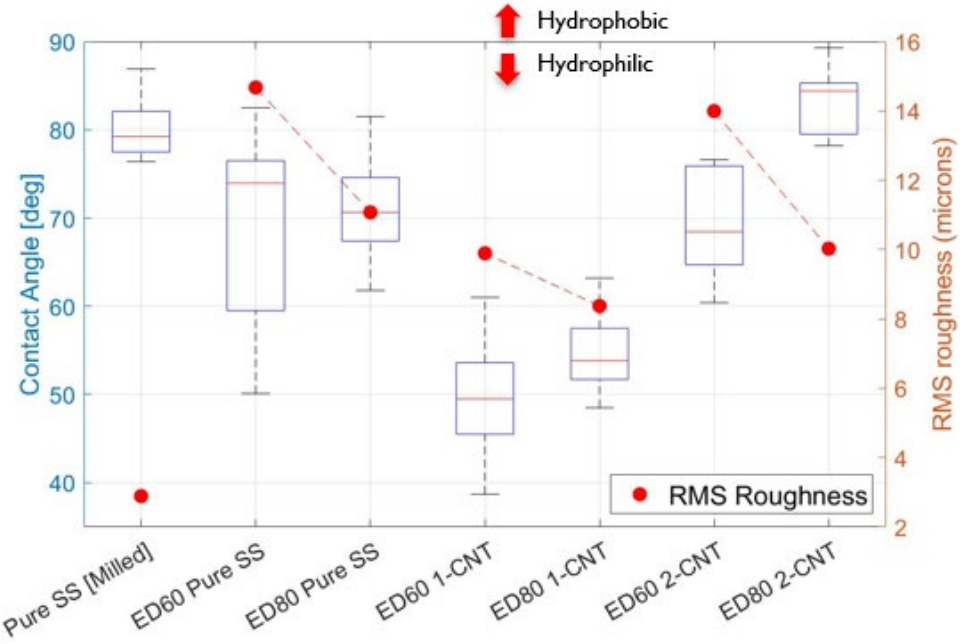

Figure 38. Sessile drop and optical profilometry data

1. Supporting Trends

When combining the sessile droplet data and roughness data, a correlation between energy density, roughness, and contact angle appears to exist. When printing at higher energy density, this amplification of the melting pool corresponds to a lower value for RMS roughness at all three concentrations. This trend is represented with red dashed lines in Figure 38. In accordance with the Wentzel equation (Eq. 2), an increase in hydrophobicity or hydrophilicity should correspond to these roughness measurements. Since all samples appeared hydrophilic in nature, it would be expected that rougher samples would have lower contact angle measurements. This is true for a majority of the samples. It is important to note that the correlation between laser energy density and wettability determined in this experiment only is applicable to material without any post-processing. The extent of energy density effects on wettability for polished samples could stand as a future work to fully explore this relationship.

Given that the sample with 2 vol. % CNT concentration had a higher contact angle than the pure stainless steel parts under similar roughness measurements, it is possible that CNT concentration could increase the wettability of a sample with all else equal. Considering the datapoints with 1 vol. % CNT dispute this claim, there is not enough evidence to support the wettability claims currently. However, data does not rule out this possibility. Further data collection must be performed with 5 vol. % CNT or other concentrations to better understand the definitive relationship between CNTs and wettability in stainless steel composites. To produce superhydrophobic samples using the pillared geometry present in the experimental section of this report, samples would likely need to be hydrophobic in natures using flat plate samples.

2. Uncertainty and Deviation

The optical profilometry data is only able to provide roughness data for a small portion of each sample, which will create some level of measurement error for both the roughness and contact angle data. As seen in the topographical maps in Figure 35, theroughness of each sample does not follow any geometric pattern. This would indicate that some areas of the sample are more or less rough than others, which would translate to

variation on contact angle measurements within the same sample. This was confirmed through qualitative observations and data deviation while conducting water droplet tests, as some portions of the samples appeared to have variation in contact angle measurements compared to the center point. For example, a hydrophobic water droplet was made on the small sample of 2 vol. % CNT stainless steel with an energy density of 80, as seen in Figure 38. Additionally, two of the corners of the large sample of 1 vol. % CNT stainless steel demonstrated very high wettability that was unable to be accurately recorded due to contact angles likely less than 15°. In order to minimize deviation, all droplets are attempted in the center of the large flat plates as well as all optical profilometry. Since the process of placing a droplet involved either manually administering water droplets or moving the MSA between measurements to dry the sample between measurements, deviation in expected in the data.

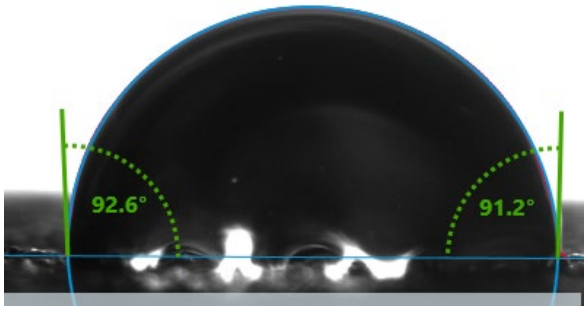

Figure 39. Hydrophobic droplet on 2 vol. % CNT ED80 sample

THIS PAGE INTENTIONALLY LEFT BLANK

V. PILLARED GEOMETRY CHARACTERIZATION

Engineered microstructures were designed and printed with the same stainless steel composites discussed in Chapter 4. These parts are discussed here in terms of wettability.

A. EOS M100 RESOLUTION TESTING

Prior to finalizing the model used when attempting to produce a superhydrophobic sample, multiple tests were conducted to determine the resolution limit of the printer. The first of these tests was to vary the size of and the spacing between pillars, with the results of this experiment shown in Figure 40. The sample produced using a pillar size of 100µm was successfully printed, but the samples produced using pillar sizes of 75µm and 50µm were unsuccessful. In the 75µm sample, the printer was able to print, but the pillared portions of the sample were fully fused into a single block and discolored. The melt pools were overlapping while conducting the print due to too close of proximity between pillars, preventing gaps from forming between them. The discoloration is likely due to many particles experiencing multiple passes from the laser and melt pool and giving the metal a marred or burned appearance. The 50µm pillared sample appears to have failed more catastrophically than the 75µm sample, as the pillar arrays were not generated. Given that the laser was melting material in even closer proximity than the 75µm sample, the negative consequences leading to a failed print were intensified. It is likely that at some point, the energy applied to the pillared array was so intense that the entire layer of powder was ejected away.

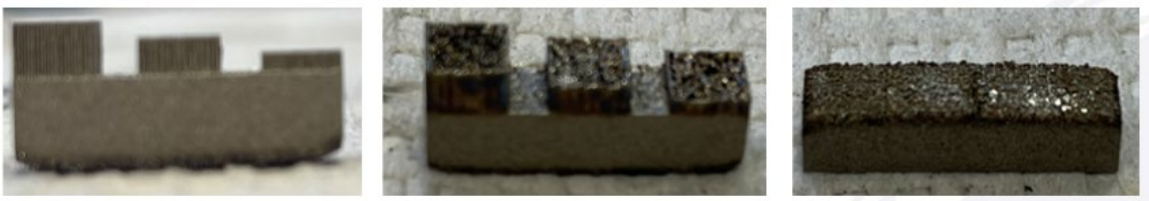

Figure 40. Pillared sample resolution test results

Although the printer is able to produce CAD models that include 100µm features as a limit, this does not show the resolution limit of the printer. In order to do so, several cones were printed, and SEM microscopy was used to determine the diameter of the tip of these cones as it theoretically approaches in exact point. The result of this experiment is a resolution limit of 160 microns, which can be seen in Figure 41. This resolution limit provides insight into the failure of the 75µm print, as it allowed no space for gaps between pillars. This experiment will also provide a reference datapoint while observing the pillared samples further.

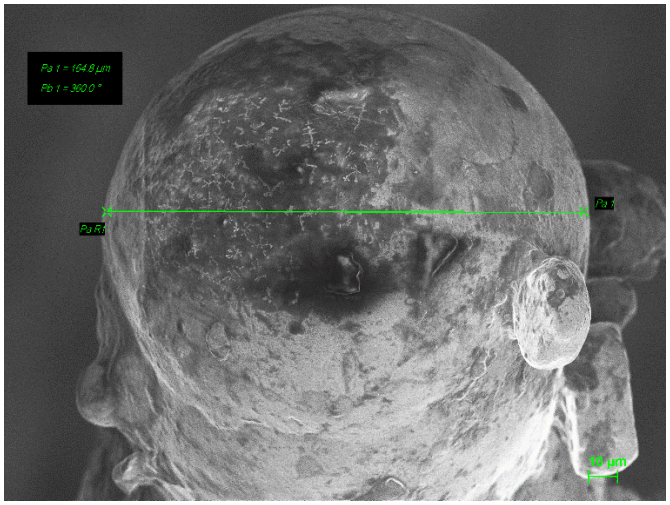

Figure 41. SEM Image of cone tip for resolution test

B. PILLARED SAMPLE MICROSCOPY

Upon successfully completing prints using a pillared geometry and various concentrations of carbon nanotubes, these samples were observed under an SEM. The resultant images from the 2 vol. % CNT sample can be seen in Figure 42. Given that the geometric features of samples at varying concentrations did not differ on the surface, images from only one sample are shown.

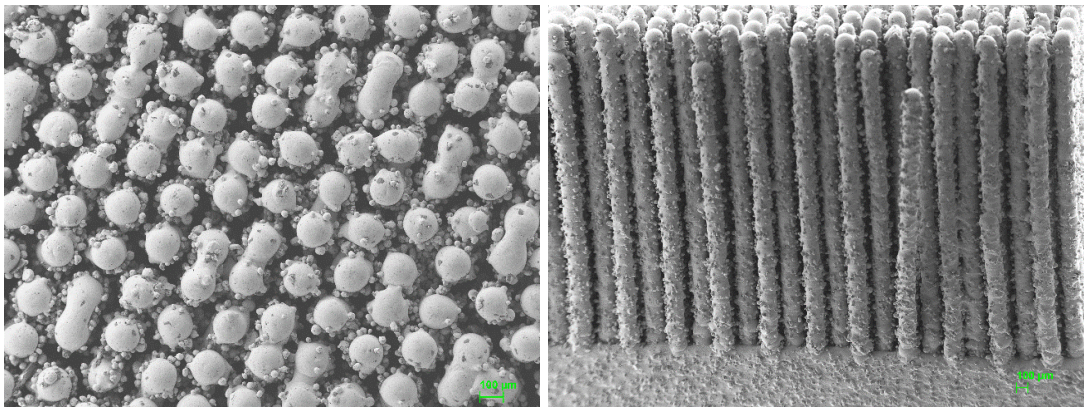

Figure 42. SEM Image of pillared sample (top view) (a) and SEM Image of pillared sample (side view) (b)

These results show several important features regarding the print that may play a role in the wettability of these samples. The first major factor is the analysis of the pillar cross sections relative to the input CAD file. The model used to generate the structure seen in Figure 42[a] is square in nature, and the width is 100 microns. Previous experimental data shows that the printed pillars are not anticipated to be under ~160μm, and Figure 42[a] confirms that that the pillar size aligned with this experiment. The green squares near the center of Figure 42[a] demonstrate the model sizing and appropriate spacing intended for the model. Since the center of the pillars and these overlayed squares are nearly aligned, the distance between pillar centers remained 200μm in both the model and print. Pillar density was maintained despite an increase in size between the model and resultant print, which led to a decrease in open space between pillars. This generates a lower porosity, which should increase the total surface area of the sample and therefore the roughness in accordance with Wentzel's equation (Eq. 2).

The increase in porosity for the sample does not guarantee an increase in roughness, as the modification of pillar shape must also be considered. Given that the laser spot is circular, as well as its melt pool, it would be expected that laser AM would not be capable of producing an exact edge. This was not something previously taken into account when creating a model, but all surfaces created using laser AM would include a fillet on all edges with a radius of half of the resolution limit. This idea is illustrated in Figure 43, demonstrating why these pillars have a circular cross section. Since it is known that the

average pillar has a diameter of 165µm, a circular cross section with a hemisphere on top, and an identical pillar height and pillar density to the original model, an analysis of total surface area was done in Table 4.

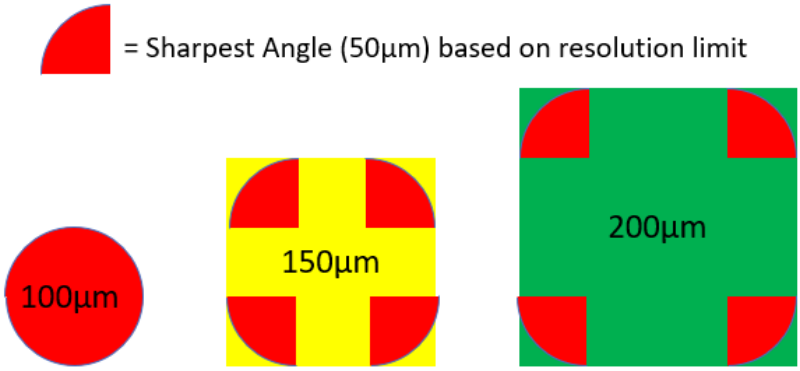

Figure 43. Explanation of circular cross sections

Table 4. Total surface area analysis

Distance into pillared sample that droplet comes to rest (µm)	**Model Porosity**	**Printed Porosity**	**Model Roughness Ratio**	**Printed Roughness Ratio**
82.5	75%	46.54%	1.8250	1.5346
100	75%	46.54%	2.0000	1.7613
150	75%	46.54%	2.5000	2.4093
200	75%	46.54%	3.0000	3.0573
500	75%	46.54%	6.0000	6.9450
1000	75%	46.54%	11.0000	13.4245

The results of this analysis show that the better performing sample for roughness in accordance with the Wentzel equation (Eq. 2) is dependent on the depth of the water droplet. If a water droplet came were allowed sink over 175µm into the sample, a similar length to width of a pillar, then the as-printed sample would be a higher performer than the model. However, a goal in superhydrophobicity would be for the sample to sink into the sample minimally and rest at the tip of the pillars, which would lead the model to be a better performer. Regardless, the margin between these are small and successfully implements what was intended for the model.

Beyond comparison to the CAD model, Figure 42 additionally presents a large quantity of particles that seem to be melted or sintered onto the pillars throughout the sample. These particles likely fused to the pillars on the outer edge of the melt pool while forming, and only a portion of the particle melted into the part. This leaves a jagged appearance to the pillars in Figure 42. These partially melted particle can be both good and bad for wettability effects depending upon their nature. If the particle is stuck to the pillar and not in contact with any other pillars, it will likely have an amplifying effect on wettability. This is the result of an increased surface area compared to if the particle was not there. If the particle is lodged between two pillars or melted to both, this would negatively impact hydrophobicity and hydrophilicity. The reason is that it could negate both roughness effects and air pocket support for superhydrophobic samples. As long as these partially melted particles do not connect pillars, they have a positive impact on the performance of the pillars.

Lastly, evidence in Figure 42 shows that several pillars were found to melt together during the print, which would have large impacts on wettability performance. The yellow circles found in Figure 42[a] and 42[b] demonstrates an example of where pillars come together, and these examples are numerous in the provided images. The connection points in the pillars are problematic as they negate the effects of the pillars underneath. When the pillars connect, any pillar surfaces or air underneath the connection point is unable to interact with the water droplet. If this connection point to very close to the tip of the pillar, this would lead to a loss of surface area. In most cases, this would minimize the potential for air pockets underneath water droplets to provide support in hydrophobic cases, as well as limit the wicking effect seen in Figure 5 for hydrophilic samples. Since the samples tested in this experiment were hydrophilic in nature, a correlation between pillar connections and wicking characteristics is expected.

To better examine this trend due to interconnectivity in the pillars, optical microscopy was performed. The longitudinal cut was made through the central array of pillars in the sample, as well as a horizontal cut through the top portion of the tall array of pillars to remove the hemispheric top. These samples were ground and polished prior to observation under the optical microscope, producing the following results in Figure 44.

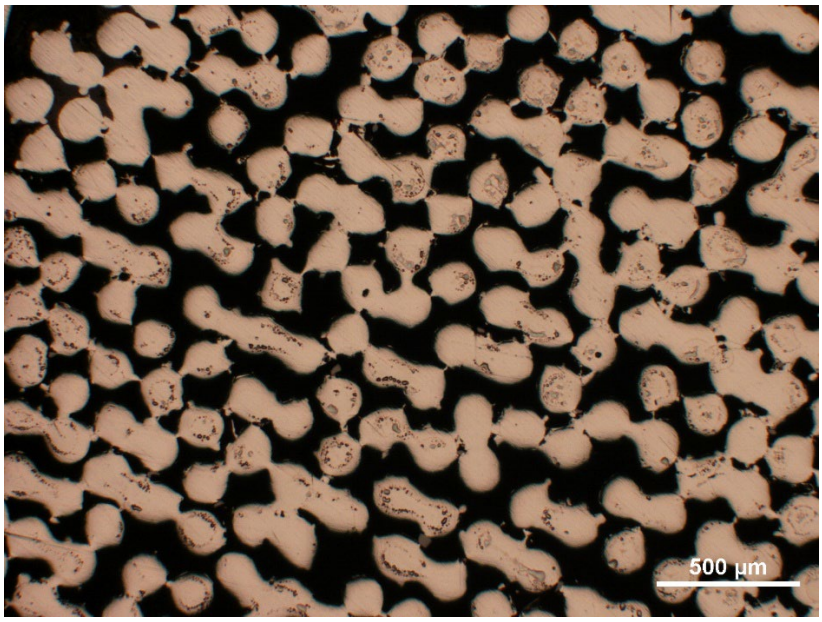

Figure 44. Optical microscope image of cross sectioned and polished 2 vol. % CNT SS composite pillars

Figure 44 shows near identical trends to those seen in Figure 42. When observing the pillars beyond the surface level, it is clear that a majority of the pillars exhibit some form of connectivity with other pillars. Many of these connections additionally appear to be aligned in the same direction, indicating that the process used to cross section the samples may have led to some of these connections. The most likely cause is the circular saw used to make the initial cross sectioning cut. However, there are still numerous examples of pillar connections that are not in the same direction as most, indicating that many of these connections are not a cause of the sample preparation.

Figure 44 shows numerous powder particles adhered to the surface of these pillars. Many of these particles appear to be within the 10–40µm range consistent with stainless steel powder, but several are significantly smaller. The likely origin of these smaller particles is small molten stainless steel droplets being ejected from the melt pool when in contact with the laser and settling on another pillar as it was being built. By seeing the presence of any necking on the particles adhered to the pillars, it is also possible to determine if the particles are melted or sintered. Based on the results of Figure 44, sintering

is present in some of the particles, but a majority of the particles were melted and fused to the pillars.

C. PILLARED SAMPLE WATER DROPLET TESTS

Upon characterizing the pillared samples based upon their geometry, sessile water droplet tests were conducted upon the samples.

1. Characterization of the Wicking Effect

Video recordings were made of water droplets deposited on each sampled pillar, the resultant videos were parsed into timelapse photos to observe variation in contact angle over time. For a superhydrophobic material, it would be expected that water droplet would slightly increase in contact angle until reaching a steady state. Based off of previous evidence, it would be expected that these samples would demonstrate the wicking effect and "sink" into the pillars in order to increase surface area until reaching a wetting state [14]. A time lapse photo of the pure stainless-steel samples is shown in Figure 45. This sample shows a water droplet demonstrating the wicking effect on a 3mm pillared array.

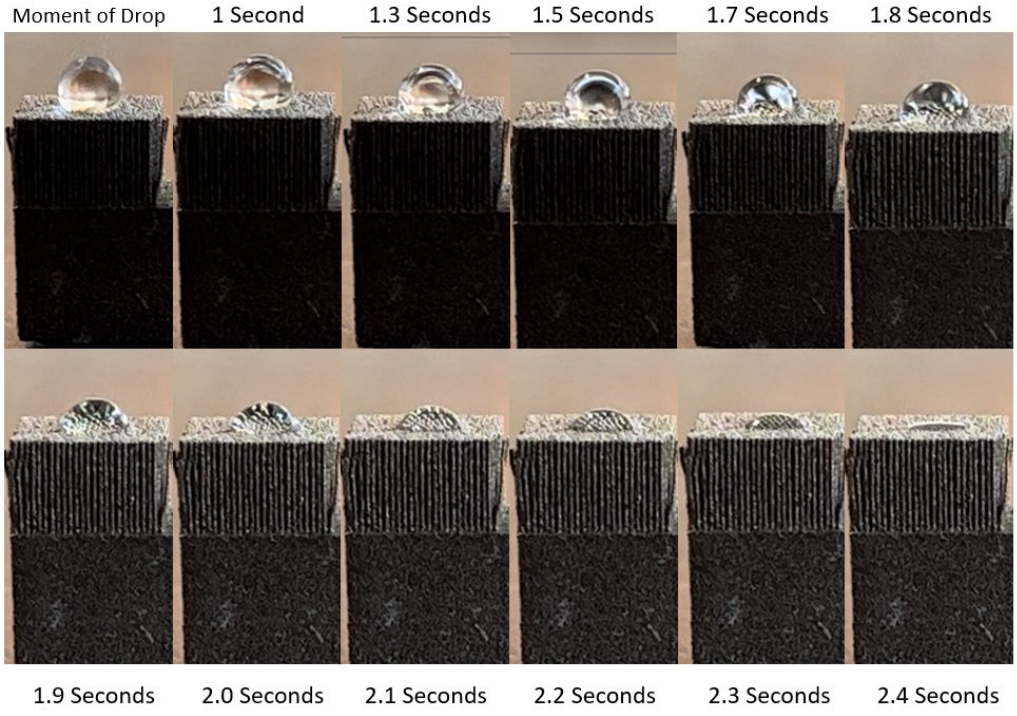

Figure 45. Pure stainless steel pillared droplet test timelapse

Figure 45 shows that the wicking effect did occur in the pure stainless steel sample. Within three seconds of administering the sessile water droplet, it appears to sink into the pillars. Combined with gravity, the droplet sinks to cover more surface area and maximize contact with the pillars. This effect would not be beneficial to corrosion resistance, as surface contact must be minimized to control corrosion. This could temporarily protect the substate if the droplet is prevented from reaching the substate, but this would be short lived due to the corrosion of the pillars themselves.

Although Figure 45 demonstrates that the stainless steel pillared samples were hydrophilic, initial observation of the samples including concentrations of carbon nanotubes was promising. Figure 46 shows the sample of stainless steel with 1 vol. % concentrations of carbon nanotubes supporting a large water droplet

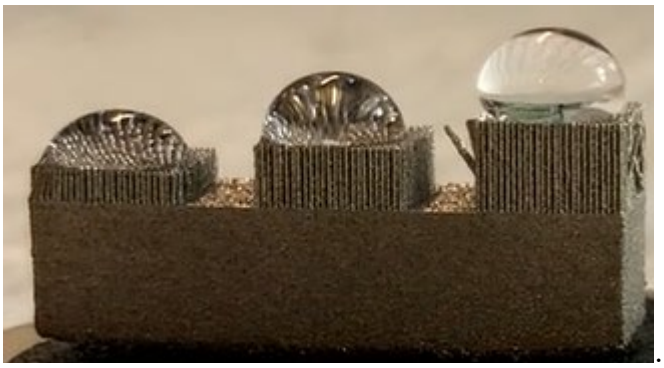

Figure 46. Initial view of 1 vol. % CNT pillared samples

The sample in Figure 46 appears to hold a water droplet in a hydrophobic state, especially the 3mm tall pillars. When conducting a test of hysteresis and rolling contact angle, the 1% pillar did not have a water roll off angle. The water droplet on this sample was able to stay fully attached to the sample even at a 180° angle, leading to the conclusion that this sample cannot be hydrophobic. Figure 47 demonstrates of portion of this roll off angle test in which the sample is held at a 90° angle while the water droplet stayed attached.

Since results from Figure 46 demonstrate hydrophobic characteristics and Figure 47 demonstrates hydrophilic characteristics, a similar video analysis of each sample was conducted. Since previous observation indicated that the water droplet was able to be

supported for short durations of time, the video analysis was conducted for approximately 30 minutes for each sample. The results of these videos are expressed in timelapse photos found in Figure 48 for a 1 vol. % CNT concentration, and Figure 49 for a 2 vol. % concentration.

Figure 47. Water roll-off angle test for 1 vol. % CNT SS sample

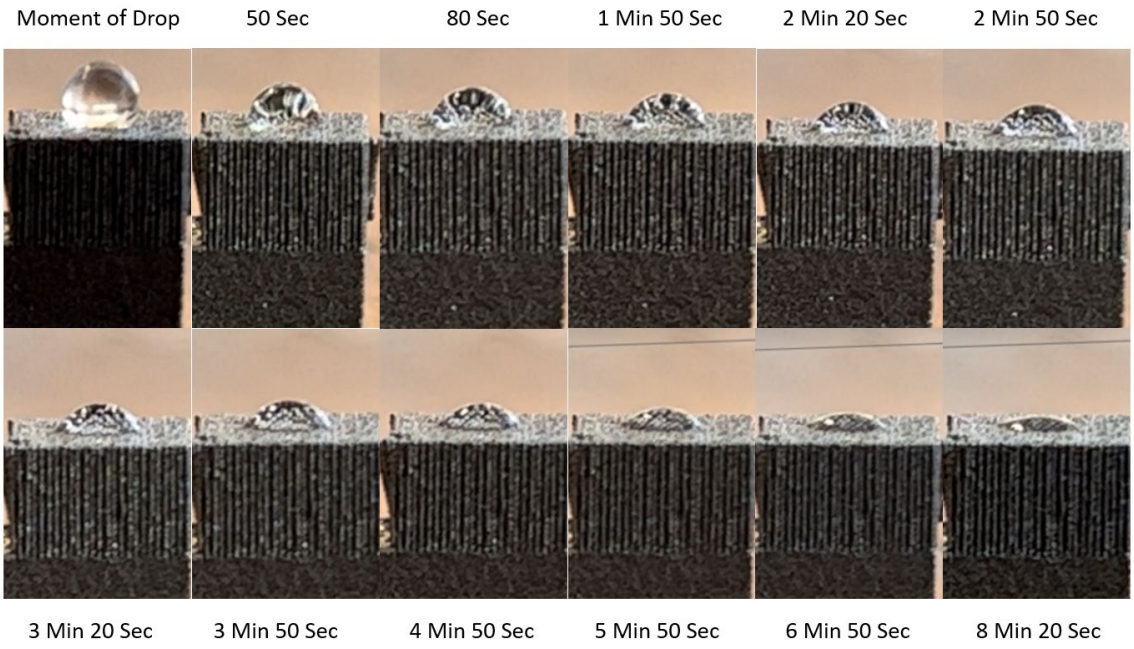

Figure 48. 1 vol. % CNT SS pillared droplet test timelapse

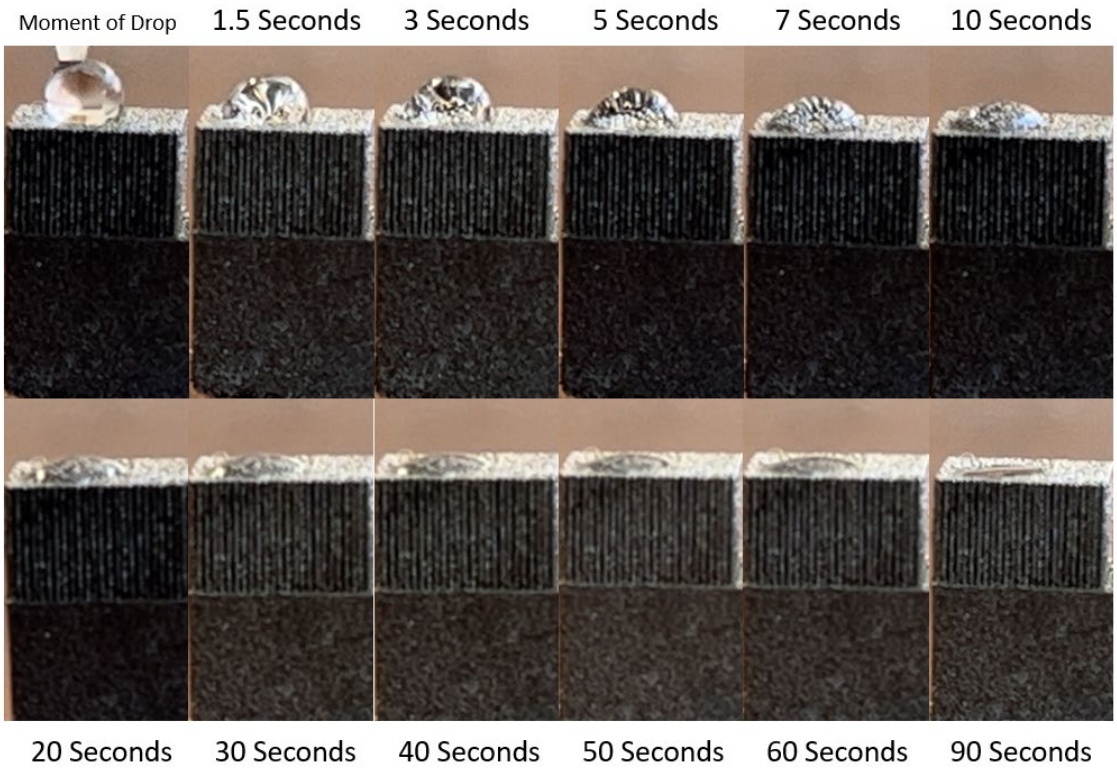

Figure 49. 2 vol. % CNT SS pillared droplet test timelapse

As these tests indicate, all pillared samples produced in this thesis demonstrate the wicking effect. The nature of these droplets sinking into the pillars is nearly identical to that of the pure stainless-steel sample, with the primary difference being the time that it takes for the sample to sink into the sample. To better understand any trends that could be present in contact angle changes with time, further video analysis was conducted for each sample. The preliminary results for these samples are shown in Figure 50. This graph demonstrates the estimated contact angle for each sample over time. These contact angle measurements were measured using the open image analysis software ImageJ, with an example of these measurements being seen in Figure 51. These measurements include a significant amount of human error, which should be taken into effect when utilizing this data beyond the establishment of general trends.

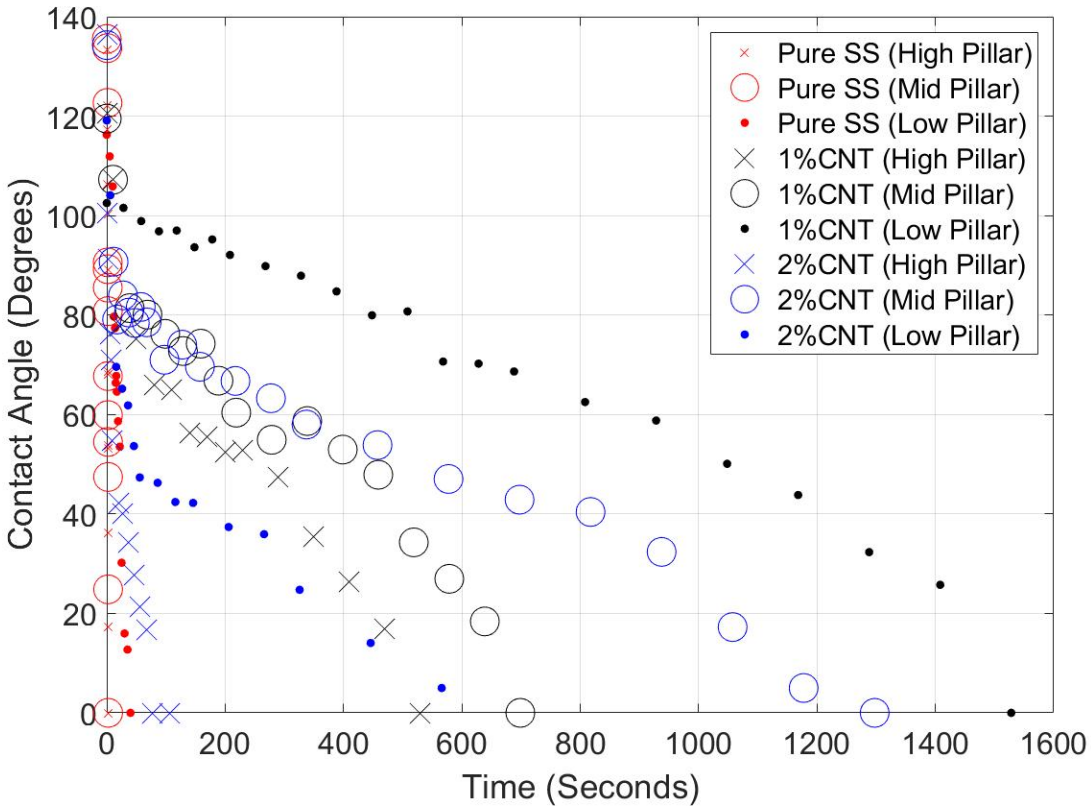

Figure 50. Trends in contact angle versus time

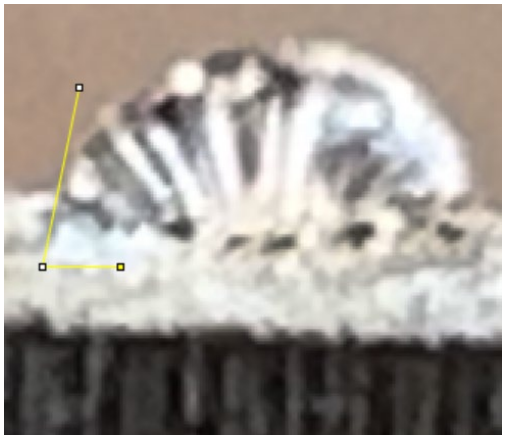

Figure 51. ImageJ image analysis contact angle example

2. Study of Wicking Effect based on Pillar Height

To determine the effects of pillar height, each concentration of carbon nanotubes was analyzed separately. When spreading the datapoints in Figure 50 into three separate

graphs, the results show the varying in performance based upon pillar height, as seen in Figure 52.

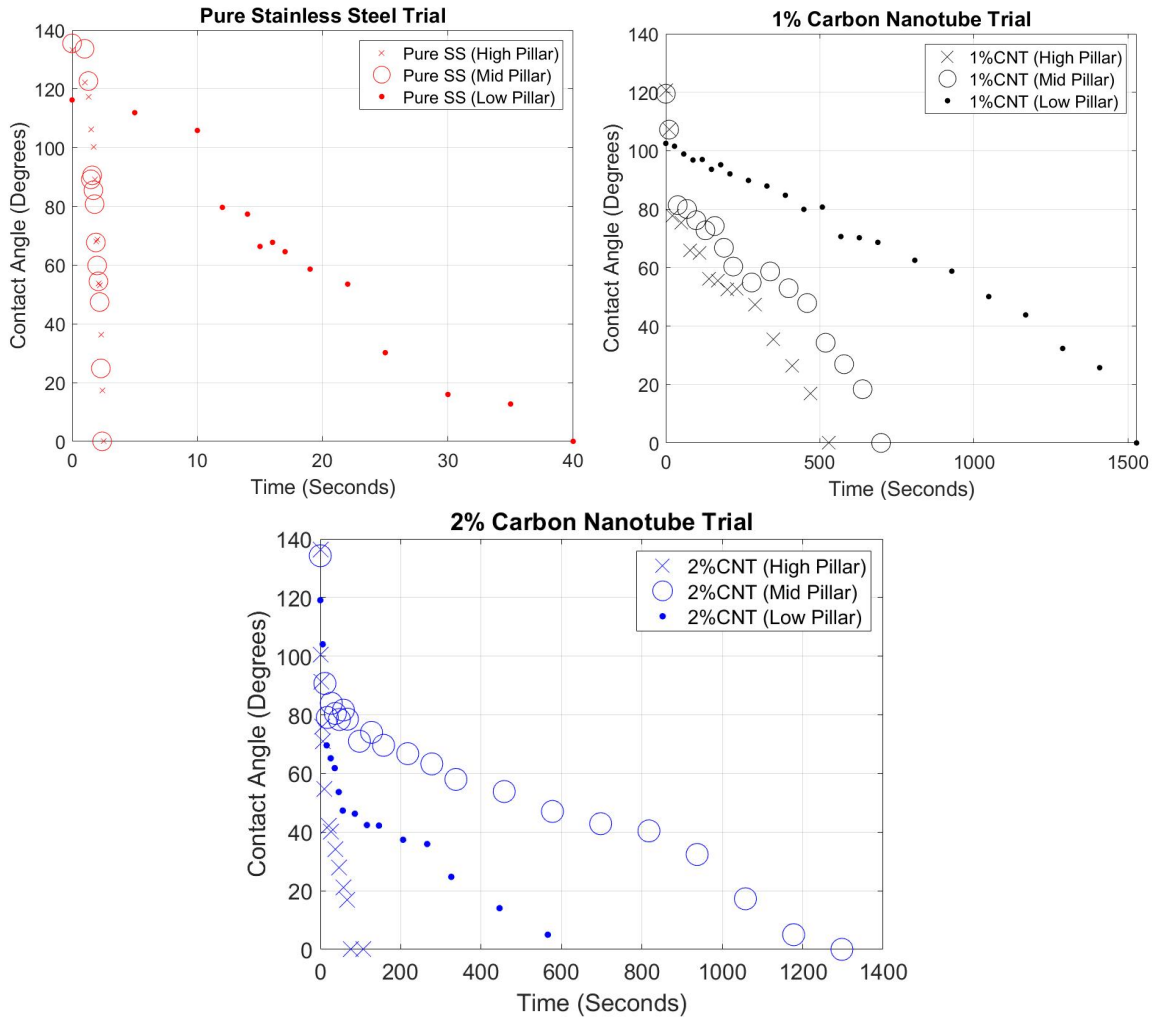

Figure 52. Effects of pillar height on contact angle

In all three powder concentrations, the highest pillar array size was the fastest to completely absorb the water droplets. This is likely the result of the highest total surface area of any pillar array. Since these high pillars were the worst performers in supporting the water droplet over time, it is unlikely that the air pockets that these taller pillars intended to provide had any effects on the droplet. This could be the result of an insufficient ratio between height and width of the pillars. More likely, however, the reason for minimal

support is the air pockets are too large. The Cassie-Baxter effect seen in nature is reliant upon pockets of air being trapped between the surface and droplet to provide support via air pressure. With larger air pockets with significant gaps for air to freely move, too little pressure is able to build up to support the droplets.

Since air pockets are not supporting the structure, it would be expected that the high pillared sample would be most susceptible to the wicking effect, followed by the middle pillar array, making the short array the best performing. This is true in two of three cases, with the exception being the 2 vol. % CNT center pillar test. The reason for this anomaly is unknown at this time, but could be due to measurement error, poor droplet placement, or a possible anomaly is the geometry of the print. This anomaly will be revisited when further observing the pillar geometry. In the pure SS and 1 vol. % tests, the lowest pillar array is not only the best performer, but it significantly outperforms the other pillar heights. The most likely reason that this is seen is because the portions of the water droplet are reaching the bottom of the pillars and the substrate, preventing them from spreading downward. Unlike the other pillared samples, the water droplet likely must spread outwards to maximize its surface area. Data from Figure 52 supports that this difference in absorption would have a large impact on time.

3. Study of Wicking Effect based on CNT concentrations

In addition to segregating the data presented in Figure 50 to observe the effects of pillar height, the same process many be used to observe the effects of carbon nanotube concentration. The results of this data segregation may be seen in Figure 53.

The graphs in Figure 53 shows the carbon nanotubes have an impact on water droplet suspension performance, although the nature of this is not clear. In every test, the pure stainless-steel samples performed worst at supporting water droplets. This trend aligns with the initial observations in which only the carbon nanotube samples were able to support a water droplet. In the lower and upper pillar datasets, the 1 vol. % carbon nanotube concentration best supported the water droplet. In the middle pillar dataset, the 2 vol. % CNT sample best supported the droplet. This is likely due to the same anomaly that was previously observed, as this difference in trend is the result of the same unexpected droplet

results on the middle pillar array of the 2 vol. % CNT sample. It is uncertain what is causing the samples with CNTs to substantially outperform traditional stainless steel in this test. Observing the geometry of the pillared cross sections could assist in explaining, but there is no conclusive cause for the variation in performance outside of the influence of CNTs at this time.

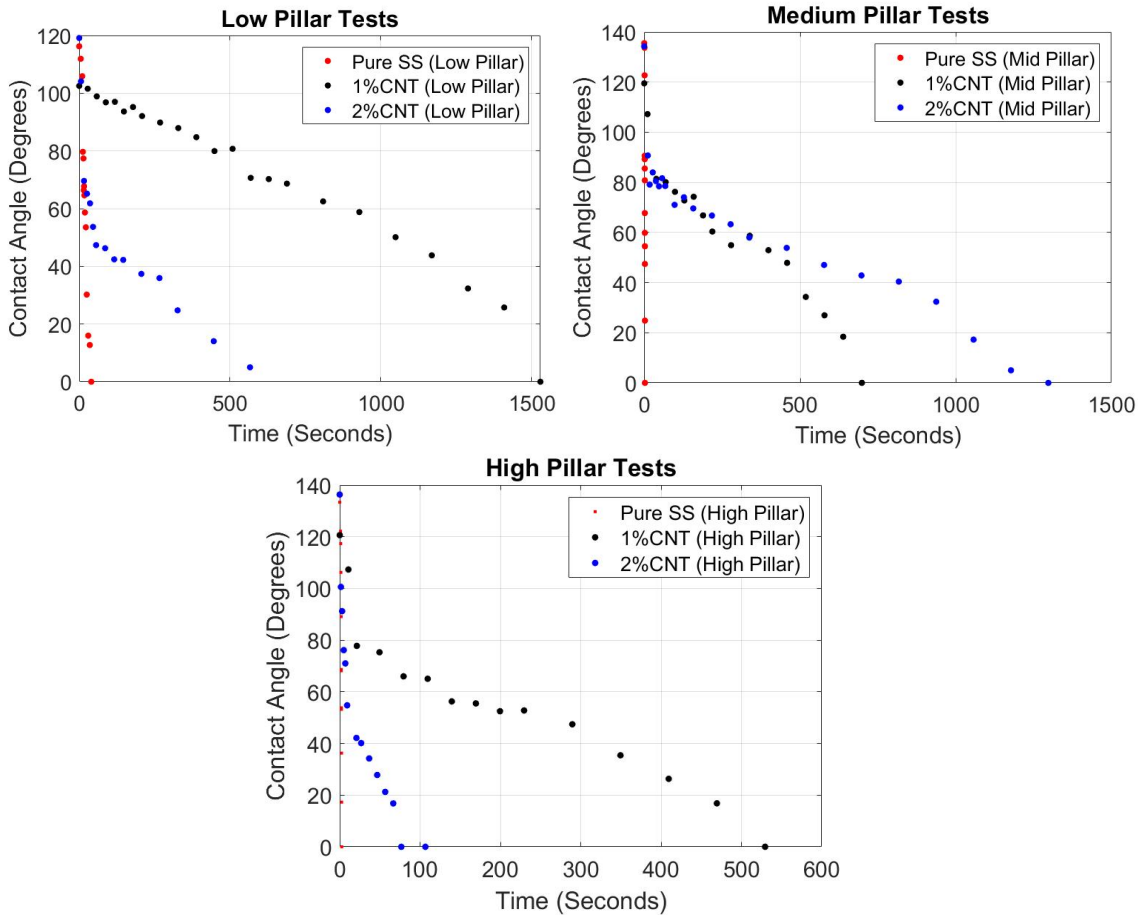

Figure 53. Effects of CNT concentration on contact angle

4. Printing Effects and Other Considerations

To further explore the trends seen in the pillared water droplet tests, the tallest array of pillars was cross sectioned, polished, and viewed under the optical microscope. The results of these images are shown in Figure 54. The images shown in Figure 54 were taken to observe any microstructure present in the samples, as well as search for any anomalies

in the printing process. The most notable tend in these images is that the minor variations in shape and pillar density, as well as pillar deformation when preparing the samples.

Figure 54. Variation in pillar geometry with CNT concentration (pure SS [a], 1 vol. % CNT [b] and 2 vol. % CNT [c])

Despite the possibility of varying pillar density in these samples being based on CNT concentration, the error and uncertainly is too significant to support such a claim. In these images, pure stainless steel has the highest porosity, followed by 2 vol. % CNT and 1 vol. % CNT, which may correlate to wicking speed. To make such an assumption, one must assume that the typical porosity of the samples is constant throughout each print, which further images indicate a variation pillar density throughout the array. Since no printer settings were changed when conducting each of these three prints, it is unlikely that this variation is based on the printer. The best way to address the possibility of printing deviation would be to re-print each sample in the same operating conditions and determine the variation in both droplet wicking time and porosity. Cutting and polishing is the most likely cause of image variation. This possibility arises due to pillar damage that incurred during cutting with the circular saw. Damage was minimized by stabilizing the sample in epoxy and thoroughly grinding and polishing the damaged layers, but patterns of pillars deforming into an oval shape in the pure and 1 vol. % composite samples indicates damage. Similarities between the optical (Figure 54[c]) and SEM images (Figure 42[a]) of the 2 vol. % sample indicates damage to this set of pillars was minimal. The reason for the 2 vol. % composite sample being damaged less in the sample preparation process is likely the result of better stabilized cutting. However, this could be the result of the composite having more favorable toughness and malleability characteristics that allowed for a cleaner

cut as a result of the CNTs. Further material characterization would need to be performed to support this claim.

D. PILLARED SAMPLE MICROSTRUCTURE OBSERVATIONS

The final experiment performed was attempting to characterize the microstructure of each of these stainless-steel composites. A section of each sample was cut and polished to reduce scratches. Etching was performed with a nitric acid solution and the samples were observed under optical microscope. The resultant microstructures are seen in Figure 55. This figure has been labelled in accordance with the building plane and building direction for each sample.

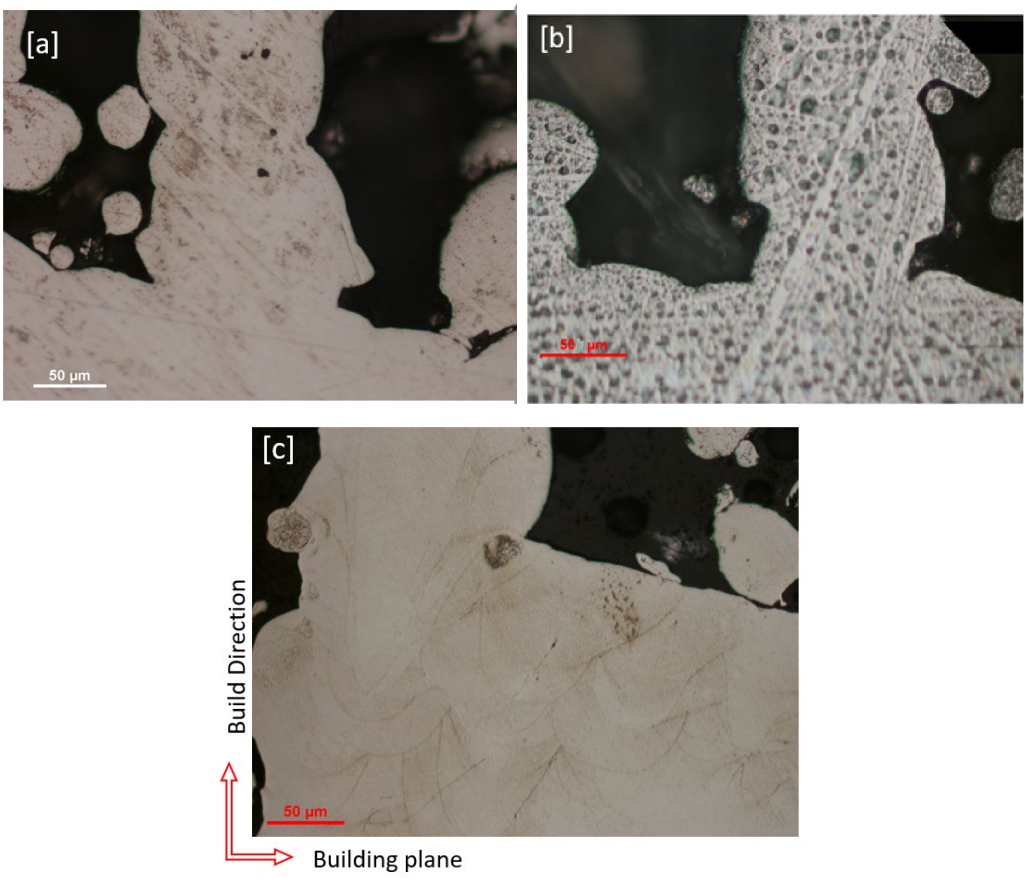

Figure 55. Pure SS microstructure (a), 1 vol. % CNT SS microstructure (b) and 2 vol. % CNT SS microstructure (c)

The results show varying microstructure when transitioning from a pure stainless steel sample [a] to the 2 vol. % CNT composites [c]. In the pure stainless steel and 1 vol. % CNT stainless steel, there is no evidence of the particles fusing together in the microstructure. This is most likely the result of insufficient etching, as all samples would be expected to demonstrate this fusing microstructure [13]. The most significant observation from these images are the presence of crescent and semicircle boundaries in the 2 vol. % sample (Figure55[c]). This structure is not found in the other sample, and most likely corresponds to the initial melting of stainless-steel composite structures. This pattern was anticipated for all samples, but only found in the 2 vol. % CNT. Since the 2 vol. % CNT composite was the only sample to show this pattern after 1 minute of etching, it is likely that the visibility of this pattern is related to the CNT concentration. Figure 55[b] shows some evidence of these welding patterns beginning to form, but it is very faint and only came after extensive etching. CNT clumping was occurring in the outer edge of particles, which may have melted to form a visible pattern upon initially melting into the sample. For future analysis, these boundaries would be a good starting point for SEM analysis to further analyze the grain boundaries of these samples and search for evidence of CNTs surviving the building process. Optical microscopy was performed at a maximum magnification of 200X on these lines, but no further analysis was able to be performed due to resolution constraints.

THIS PAGE INTENTIONALLY LEFT BLANK

VI. CONCLUSIONS

Although this thesis was unable to accomplish its initial goal of developing superhydrophobic stainless steel composites, it still gave valuable insights into the characteristics necessary to make superhydrophobic metals possible in the future. Through SEM analysis of the milled powders and successful subsequent printing, it was shown that CNTs can effectively mixed with stainless steel to form useable composite. Sessile drop experiments revealed that the implementation of CNTs at 1 vol. % or 2 vol. % concentration was unable to produce hydrophobicity, but the results were not far off and show promise for the future with higher concentrations. Optical profilometry showed an increase in roughness led to a decrease in contact angle, i.e., rougher samples were more hydrophilic. Given the hydrophilic results in the sessile drop experiment, this result is anticipated based upon the Wentzel equation (2). SEM images reveal the resolution of the EOS M100 SLM printer to be around 150μm for pillars, as well as several occurrences of partial melting and interconnectivity among the pillars. Since a 100μm resolution was anticipated, the model would likely be modified in future tests to better promote air pocket support. Sessile water droplet tests showed the pillars did not support water droplets over an extended period time, but rather demonstrates the wicking effect at various speeds. The wicking effect was anticipated based upon the hydrophilic nature of the materials, but the variation in speed could be the result of CNT concentration and pillar porosity. Optical microscopy of these samples revealed variation in porosity as well as variations in microstructure. Although weld lines was expected in all samples, they were only visible in the 2 vol. % model. This may be due to the residual carbon from carbon nanotubes building up in the weld lines and becoming more visible.

With these insights, it is plausible that superhydrophobic stainless steel composites can be produced through AM. If the as-printed roughness impact the 2 vol. % CNT samples as prevalently as the pure stainless steel samples, the 2 vol. % CNT sample is able to perform with a contact angle above 85°. Under smooth conditions, a material must only achieve a contact angle greater than 90° for superhydrophobicity to be possible. If the transition from 2 vol. % CNT to 5 vol. % CNT has comparable impacts as the transition

from pure SS to 2 vol. % CNT, hydrophobic flat surfaces would be likely to occur. The experimental pillared model was designed under the premise of a 100μm resolution limit, but adjustments made in consideration of the actual 150μm limit could better promote the air pockets necessary for superhydrophobic behavior. Despite not achieving superhydrophobic results in this thesis, the necessary background has been established to achieve such results in the near future.

VII. FUTURE WORK

There are potential modifications that could be made in both material composition and printing methods that could improve performance. This chapter will outline three options of future study that should be facilitated in the future to continue to develop the study of superhydrophobic metals and composites.

A. HIGHER CONCENTRATION CNT PRINTING

Despite the development of 316L stainless steel powder with a 5% volumetric concentration of carbon nanotubes, it was unable to be used for printing in this thesis. Using the previous printing parameters and models, one could complete a printing cycle using the already fabricated powder to determine the impact of the concentration increase. Previous studies [23] have shown that successfully printing with this higher concentration of CNTs is possible. The current scope of this thesis only utilizes three different concentrations of carbon nanotubes with one of being used as a pure SS reference. This makes the interpolation of trends difficult to determine with accuracy. Adding another datapoint would be beneficial in validating data seen in this thesis, as well as possibly generating a powder capable of achieving hydrophobicity regardless of geometry. Given the increase in contact angle between the 2 vol. % CNT samples and the 1 vol. % CNT samples, and the current top measurements being above 80° in several cases, samples using 5 vol. % CNT could cross the threshold for hydrophobicity. Even if hydrophobic results are not achieved with this method, it would still serve as a valuable datapoint.

B. EXPLORATION OF ALTERNATIVE PRINTING METHODS

Although selective laser melting was chosen as the preferred additive manufacturing method in this experiment, further testing with other manufacturing methods should be explored. The EOS M100 printer in this experiment was shown to operate at a resolution of approximately 150μm, which was shown to be insufficient for producing supporting air pockets in a tightly packed array. The powder itself likely limits the resolution to approximately 40μm based on the size of particles, but any additional increase in resolution is primarily based on the melting mechanism of the printer. There is

no promise of this 40μm resolution being sufficiently small for achieving air pocket support in pillars, but it would be worthwhile to explore its potential. There are several printing mechanisms available that are able achieve resolutions below 100μm. For example, many systems that use a direct electron or ion beam rather than a laser are able to operate at a much lower resolution [13]. A recommendation for such a study would be to experimentally determine the resolution limit of the printer being used, then build a model with pillars that are two times the resolution away from one another (center to center) and a pillar size 20μm smaller than the experimental resolution limit to take into effect partially melted powder particles.

C. ALTERNATIVE NANOMATERIAL POWDERS

Although carbon nanotubes showed promise in literature as an affordable nanomaterial to improve wettability characteristics, other nanomaterials could be explored. Nanomaterials is a fast-developing field in the study of material science and the full effects of alloying different materials with nanomaterials is still largely unexplored. In particular, the effects on wettability of different nanomaterials in 316L stainless steel. There is a possibility that other nanomaterials could increase wettability in ways that were not previously anticipated. Most studies that focus on wettability and nanomaterials tend of emphasize the orientation of the nanomaterials on the surface but creating these composites in powder form prior to assembling creates a largely different impact on material performance. Carbon nanotubes did not generate hydrophobicity under 2% concentration by volume, but this has no indication for other nanomaterials such as graphene nanoplatelets, silicone-based nanoparticles, or B_4C nanoparticles.

As a final note, the whole subject of engineering superhydrophobic stainless steel composites is still largely unexplored. The methods used or suggested in this thesis are not meant to be exhaustive in nature, but rather an introduction to one of many novel attempts at producing superhydrophobicity. This method attempts to use a particular nanomaterial and particular printing method, chosen primarily on the prior research and available resources. There are other approaches that could be explored and any future work with the potential for producing superhydrophobic metals that is more environmentally friendly,

safer, cheaper, usable with a wider scope of geometries, or faster could be very beneficial future work.

THIS PAGE INTENTIONALLY LEFT BLANK

APPENDIX. ADDITIONAL DATA

The following results are for the milled pure stainless-steel sample

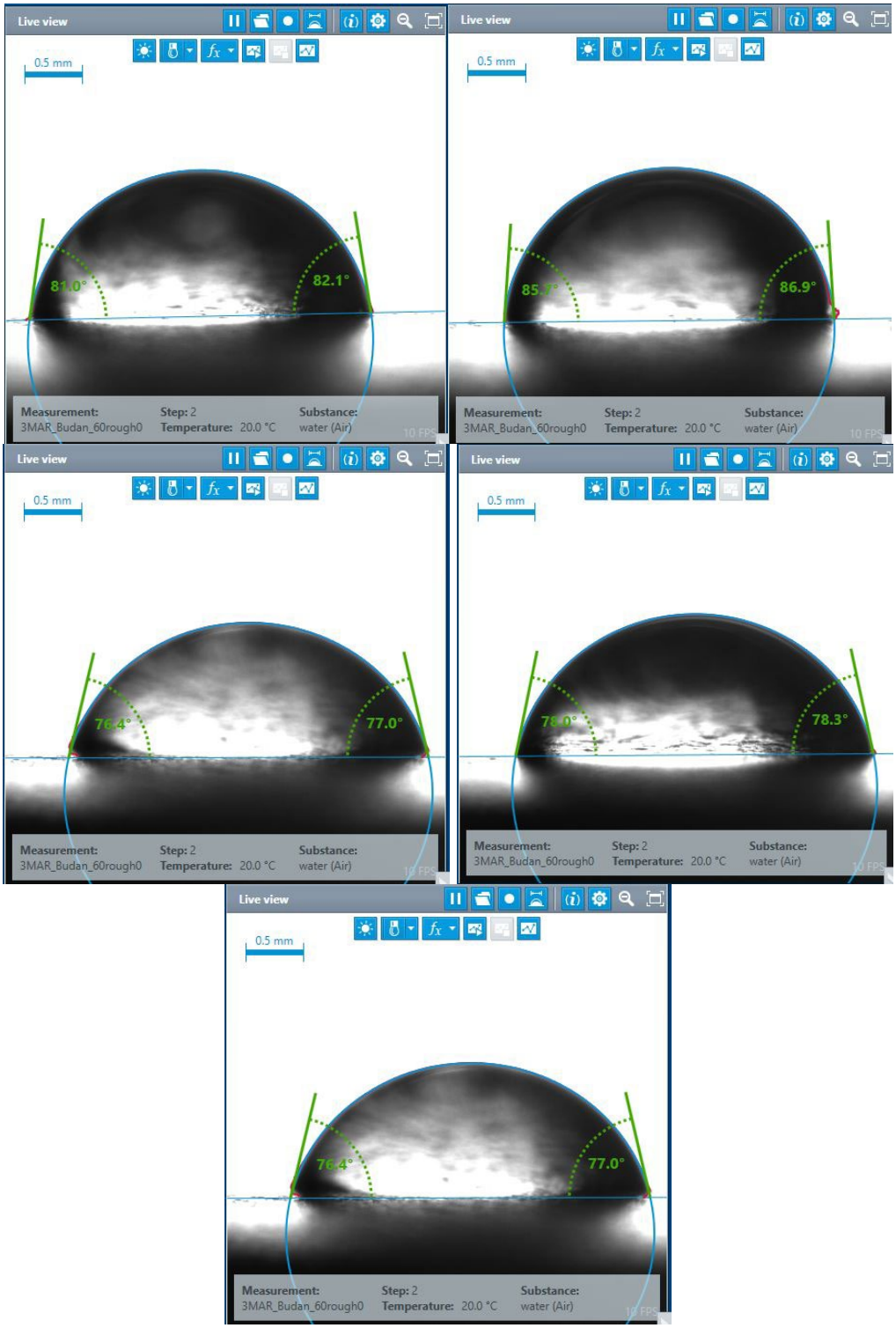

The following results are for the 3D-Printed ED-60 pure stainless-steel sample

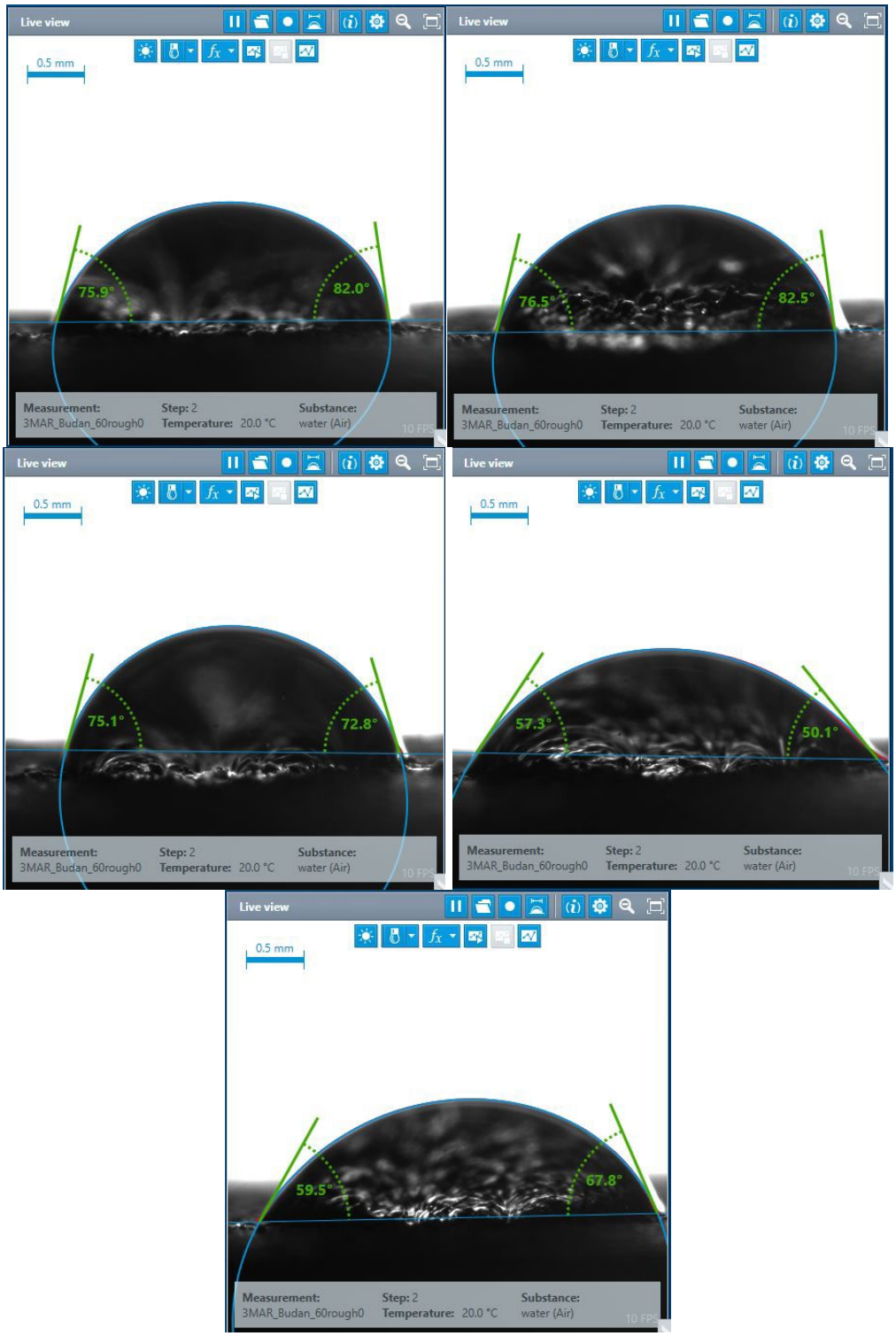

The following results are for the 3D-Printed ED-80 pure stainless-steel sample

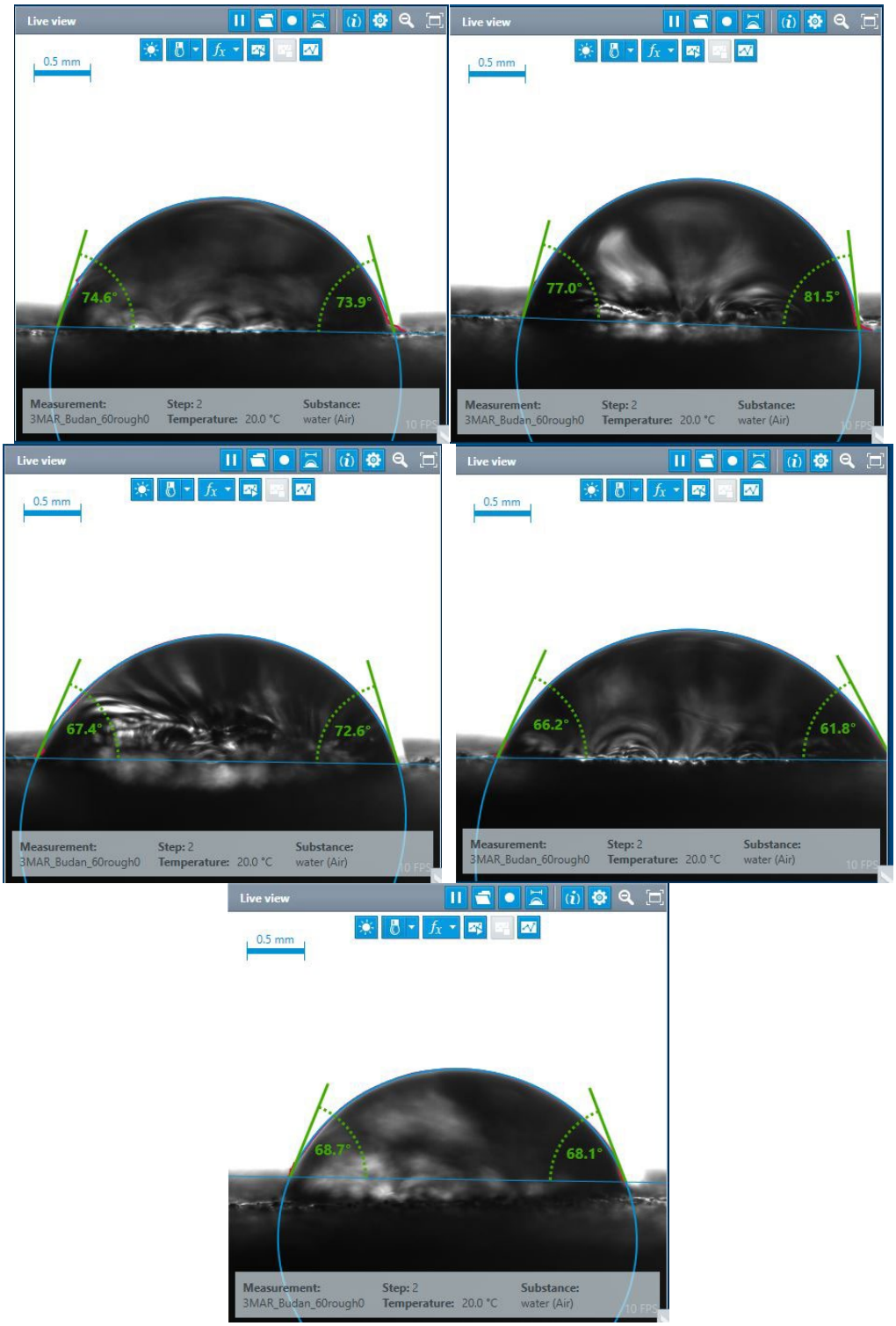

The following results are for the 3D-Printed ED-60 1 vol. % CNT stainless-steel sample

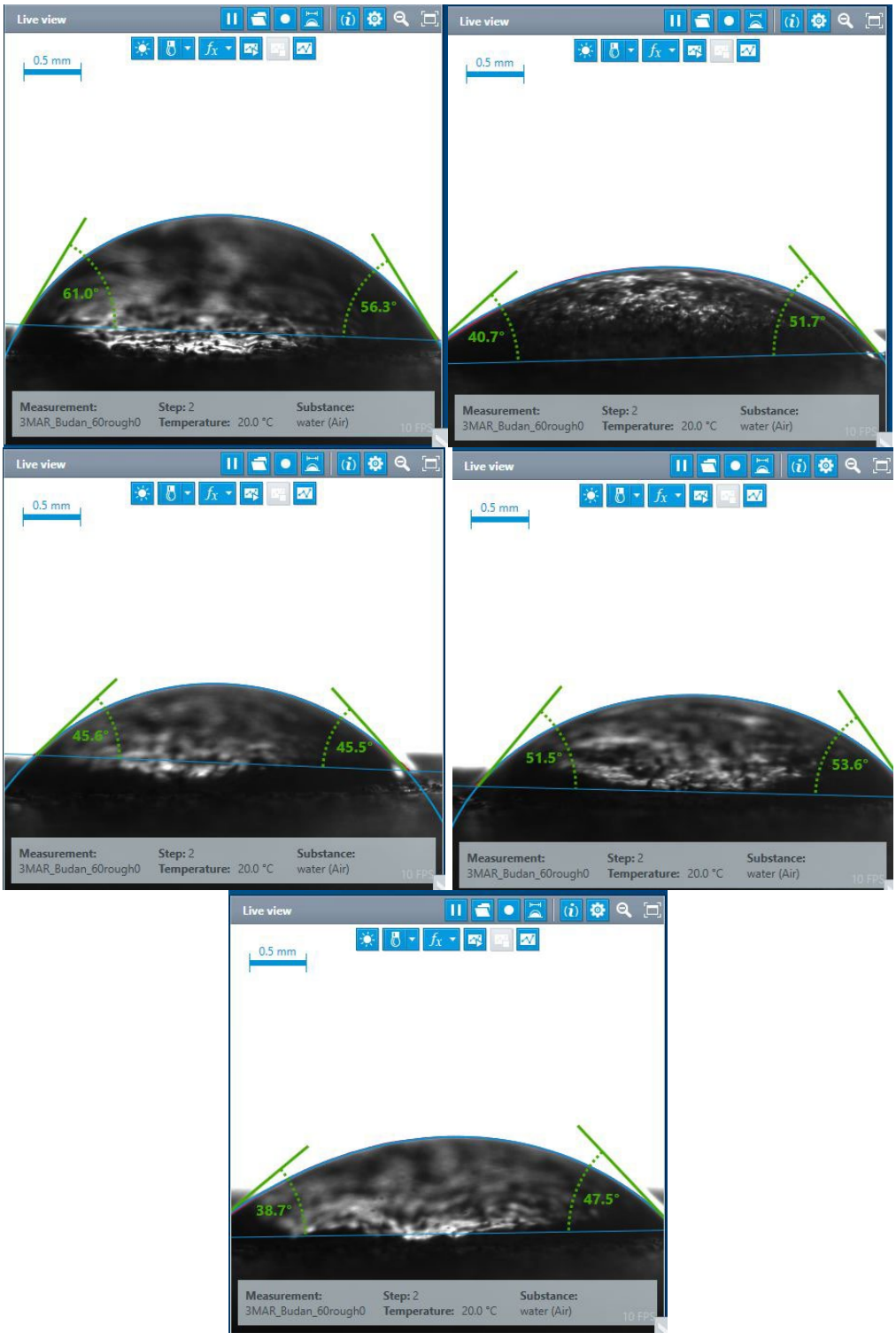

The following results are for the 3D-Printed ED-80 1 vol. % CNT stainless-steel sample

The following results are for the 3D-Printed ED-60 2 vol. % CNT stainless-steel sample

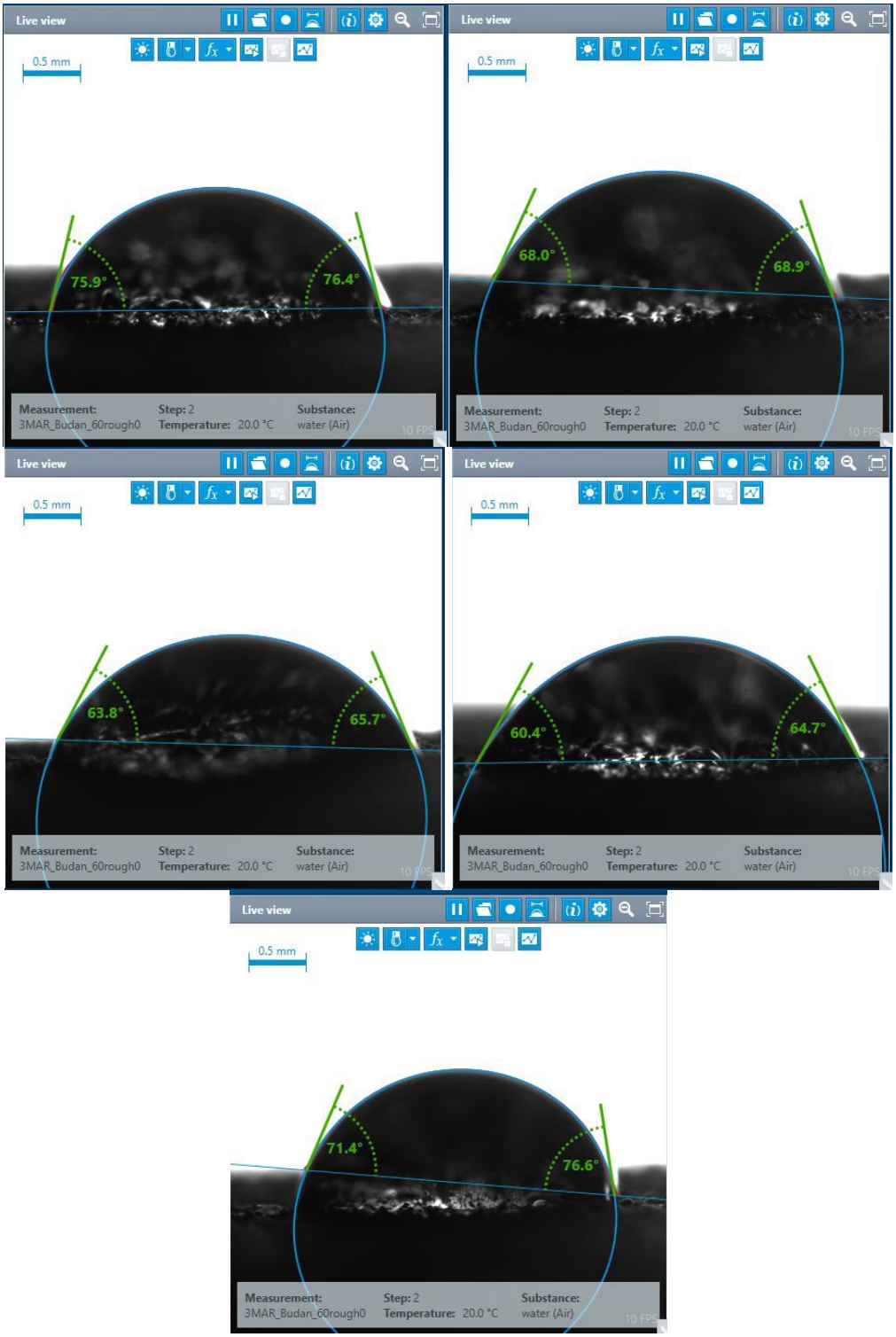

The following results are for the 3D-Printed ED-80 2 vol. % CNT stainless-steel sample

THIS PAGE INTENTIONALLY LEFT BLANK

LIST OF REFERENCES

[1] G. Koch, J. Varney, N. Thompson, O. Moghissi, M. Gould, and J. Payer, "International measures of prevention, application, and economics of corrosion technologies study," NACE International, 2016. [Online]. Available: http://impact.nace.org/economic-impact.aspx

[2] E. McCafferty, "Chapter 1 Societal aspects of corrosion," in *Introduction to Corrosion Science*, New York, NY, USA: Springer, 2010, pp. 1–11.

[3] United States Government Accountability Office. "Defense management observations on changes to the reporting structure for DOD's corrosion office and its implementation of GAO recommendations," United States Government Accountability Office, United States Congress, May 2019.

[4] E. McCafferty, "Chapter 2 Getting started on the basics," in *Introduction to Corrosion Science*, New York, NY, USA: Springer, 2010, pp. 13–32.

[5] E. Vazirnasab, R. Jafari, and G. Momen, "Application of superhydrophobic caotings as a corrosion barrier: A review," *Surf. Coat. Technol.*, vol. 341, pp. 40–56, Nov. 2017.

[6] D. Zhang, L. Wang, H. Qian, and X. Li, "Superhydrophobic surfaces for corrosion protection: a review of recent progresses and future directions," *J. Coat. Technol. Res.*, vol. 13, no. 1, pp. 11–29, Jan. 2016, doi: 10.1007/s11998-015-9744-6.

[7] W. Liu, Q. Xu, J. Han, X. Chen, and Y. Min, "A novel combination approach for the preparation of superhydrophobic surface on copper and the consequent corrosion resistance," *Corros. Sci.*, vol. 110, pp. 105–113, Apr. 2016.

[8] J. Zhu and Hu, XiaoFang, "A novel route for fabrication of the corrosion-resistant superhydrophobic surface by turning operation," *Surf. Coat. Technol.*, vol. 313, pp. 294–298, Feb. 2017.

[9] M. A. Samaha, H. V. Tafreshi, and M. Gad-el-Hak, "Superhydrophobic surfaces: from the lotus leaf to the submarine," *Comptes Rendus Mécanique*, vol. 340, no. 1–2, pp. 18–34, Jan. 2012, doi: 10.1016/j.crme.2011.11.002.

[10] A. Rüttgers *et al.*, "Simulation of the oil storage process in the scopa of specialized bees," *Comput. Fluids*, vol. 119, pp. 115–130, Sep. 2015, doi: 10.1016/j.compfluid.2015.06.029.

[11] National Aviation Academy. "How does aircraft deicing work?," Dec. 08, 2021 [Online]. Available: https://www.naa.edu/aircraft-deicing/.

[12] E. Hughes, “Advances in hydrophilic and hydrophobic coatings for medical devices,” *Medical Design Briefs*, Oct. 01, 2017. [Online]. Available: https://www.medicaldesignbriefs.com/component/content/article/mdb/features/articles/27725.

[13] E. Gunduz, “Lecture 9: Selective Laser Sintering/Melting (SLS, SLM) Powder Bed Fusion,” class notes for ME4901: Additive Manufacturing Methods, Dept. of Mechanical and Aerospace Eng., Naval Postgraduate School, Monterey, CA, USA, Winter 2022.

[14] J. T. Simpson, S. R. Hunter, and T. Aytug, “Superhydrophobic materials and coatings: a review,” *Rep. Prog. Phys.*, vol. 78, no. 8, p. 086501, Jul. 2015, doi: 10.1088/0034-4885/78/8/086501.

[15] H. J. Ensikat, P. Ditsche-Kuru, C. Neinhuis, and W. Barthlott, “Superhydrophobicity in perfection: the outstanding properties of the lotus leaf,” *Beilstein J. Nanotechnol.*, vol. 2, pp. 152–161, Mar. 2011, doi: 10.3762/bjnano.2.19.

[16] B. R. Sedai, B. K. Khatiwada, H. Mortazavian, and F. D. Blum, “Development of superhydrophobicity in fluorosilane-treated ditomaceous earth polymer coatings,” *Appl. Surf. Sci.*, vol. 386, pp. 178–186, Jun. 2016.

[17] N. M. Oliveira, R. L. Reis, and J. F. Mano, “Superhydrophobic surfaces engineered using diatomaceous earth,” *ACS Appl. Mater. Interfaces*, vol. 5, no. 10, pp. 4202–4208, May 2013, doi: 10.1021/am4003759.

[18] H. J. Perera, B. K. Khatiwada, A. Paul, H. Mortazavian, and F. D. Blum, “Superhydrophobic surfaces with silane-treated diatomaceous earth/resin systems,” *J. Appl. Polym. Sci.*, vol. 133, no. 41, Nov. 2016, doi: 10.1002/app.44072.

[19] S. S. Latthe *et al.*, “A mechanically bendable superhydrophobic steel surface with self-cleaning and corrosion-resistant properties,” *J. Mater. Chem. A*, vol. 3, no. 27, pp. 14263–14271, 2015, doi: 10.1039/C5TA02604K.

[20] A. Milionis, C. Noyes, E. Loth, and I. S. Bayer, “Superhydrophobic 3D printed surfaces by dip-coating,” in *Nanotech 2014: Technical Proceedings of the 2014 NSTI Nanotechnology Conference and Expo, June 15–18, 2014, Gaylor National Resort & Convention Center, Washington, U.S.A An Interdisciplinary Integrative Forum on Nanotechnology, Microtechnology, Biotechnology and Cleantechnology*, Boston, MA, USA: CRC press, 2014.

[21] F. Hizal *et al.*, “Nanoengineered superhydrophobic surfaces of aluminum with extremely low bacterial adhesivity,” *ACS Appl. Mater. Interfaces*, vol. 9, no. 13, pp. 12118–12129, Apr. 2017, doi: 10.1021/acsami.7b01322.

[22] T. Verho, C. Bower, P. Andrew, S. Franssila, O. Ikkala, and R. H. A. Ras, "Mechanically durable superhydrophobic surfaces," *Adv. Mater.*, vol. 23, no. 5, pp. 673–678, Feb. 2011, doi: 10.1002/adma.201003129.

[23] H. Yin, J. Yang, Y. Zhang, L. Crilly, R. L. Jackson, and X. Lou, "Carbon nanotube (CNT) reinforced 316L stainless steel composites made by laser powder bed fusion: microstructure and wear response," *Wear*, vol. 496–497, p. 204281, May 2022, doi: 10.1016/j.wear.2022.204281.

[24] G. Kaur, A. Marmur, and S. Magdassi, "Fabrication of superhydrophobic 3D objects by Digital Light Processing," *Addit. Manuf.*, vol. 36, p. 101669, Dec. 2020, doi: 10.1016/j.addma.2020.101669.

[25] C. Luhrs, "Nanomaterials Introduction," class notes for MS4601: Fabrication, Characterization and Application of Nanomaterials, Dept. of Mechanical and Aerospace Eng., Naval Postgraduate School, Monterey, CA, USA, Spring 2022.

[26] S. F. Ahmed, M. Khalid, W. Rashmi, A. Chan, and K. Shahbaz, "Recent progress in solar thermal energy storage using nanomaterials," *Renew. Sustain. Energy Rev.*, vol. 67, pp. 450–460, Jan. 2017, doi: 10.1016/j.rser.2016.09.034.

[27] J. Zhu, "Clustered ribbed-nanoneedle structured copper surfaces with high-efficiency dropwise condensation heat transfer performance," *Am. Chem. Soc. Appl. Mater. Interfaces*, no. 7, pp. 10660–10665, May 2015.

[28] T. Krupenkin, J. A. Taylor, P. Kolodner, and M. Hodes, "Electrically tunable superhydrophobic nanostructured surfaces," *Bell Labs Tech. J.*, vol. 10, no. 3, pp. 161–170, Jul. 2005.

[29] B. D'Urso, J. T. Simpson, and M. Kalyanaraman, "Emergence of superhydrophobic behavior on vertically aligned nanocone arrays," *Appl. Phys. Lett.*, vol. 90, no. 4, p. 044102, Jan. 2007, doi: 10.1063/1.2433039.

[30] C.-H. Choi and C.-J. Kim, "Fabrication of a dense array of tall nanostructures over a large sample area with sidewall profile and tip sharpness control," *Nanotechnology*, vol. 17, no. 21, pp. 5326–5333, Nov. 2006, doi: 10.1088/0957-4484/17/21/007.

[31] Z. Wang, C. Lopez, A. Hirsa, and N. Koratkar, "Impact dynamics and rebound of water droplets on superhydrophobic carbon nanotube arrays," *Appl. Phys. Lett.*, vol. 91, no. 2, p. 023105, Jul. 2007, doi: 10.1063/1.2756296.

[32] C. Sciancalepore, L. Gemini, L. Romoli, and F. Bondioli, "Study of the wettability behavior of stainless steel surfaces after ultrafast laser texturing," *Surf. Coat. Technol.*, vol. 352, pp. 370–377, Oct. 2018, doi: 10.1016/j.surfcoat.2018.08.030.

[33] M. Yakout, M. A. Elbestawi, and S. C. Veldhuis, “Density and mechanical properties in selective laser melting of Invar 36 and stainless steel 316L,” *J. Mater. Process. Technol.*, vol. 266, pp. 397–420, Apr. 2019, doi: 10.1016/j.jmatprotec.2018.11.006.

[34] Cheaptubes. “Multi walled carbon nanotubes 10–20nm,” [Online]. Available: https://www.cheaptubes.com/product/multi-walled-carbon-nanotubes-10-20nm/

[35] S. Lauren, “How to measure surface free energy?,” *Surface Science Blog*, Apr. 06, 2017. https://www.biolinscientific.com/blog/how-to-measure-surface-free-energy

INITIAL DISTRIBUTION LIST

1. Defense Technical Information Center
   Ft. Belvoir, Virginia

2. Dudley Knox Library
   Naval Postgraduate School
   Monterey, California